NASA/TM—2019-220012 AIAA–2018–3492

Independent Effects of Reynolds Number and Mach Number on Aerodynamics of an Iced Swept Wing

Andy P. Broeren
Glenn Research Center, Cleveland, Ohio

Sam Lee
Vantage Partners, LLC, Brook Park, Ohio

Brian S. Woodard
University of Illinois at Urbana-Champaign, Urbana, Illinois

Christopher W. Lum
University of Washington, Seattle, Washington

Timothy G. Smith
Federal Aviation Administration, William J. Hughes Technical Center, Egg Harbor Township, New Jersey

July 2019

NASA STI Program . . . in Profile

Since its founding, NASA has been dedicated to the advancement of aeronautics and space science. The NASA Scientific and Technical Information (STI) Program plays a key part in helping NASA maintain this important role.

The NASA STI Program operates under the auspices of the Agency Chief Information Officer. It collects, organizes, provides for archiving, and disseminates NASA's STI. The NASA STI Program provides access to the NASA Technical Report Server—Registered (NTRS Reg) and NASA Technical Report Server—Public (NTRS) thus providing one of the largest collections of aeronautical and space science STI in the world. Results are published in both non-NASA channels and by NASA in the NASA STI Report Series, which includes the following report types:

- TECHNICAL PUBLICATION. Reports of completed research or a major significant phase of research that present the results of NASA programs and include extensive data or theoretical analysis. Includes compilations of significant scientific and technical data and information deemed to be of continuing reference value. NASA counter-part of peer-reviewed formal professional papers, but has less stringent limitations on manuscript length and extent of graphic presentations.

- TECHNICAL MEMORANDUM. Scientific and technical findings that are preliminary or of specialized interest, e.g., "quick-release" reports, working papers, and bibliographies that contain minimal annotation. Does not contain extensive analysis.

- CONTRACTOR REPORT. Scientific and technical findings by NASA-sponsored contractors and grantees.

- CONFERENCE PUBLICATION. Collected papers from scientific and technical conferences, symposia, seminars, or other meetings sponsored or co-sponsored by NASA.

- SPECIAL PUBLICATION. Scientific, technical, or historical information from NASA programs, projects, and missions, often concerned with subjects having substantial public interest.

- TECHNICAL TRANSLATION. English-language translations of foreign scientific and technical material pertinent to NASA's mission.

For more information about the NASA STI program, see the following:

- Access the NASA STI program home page at http://www.sti.nasa.gov

- E-mail your question to help@sti.nasa.gov

- Fax your question to the NASA STI Information Desk at 757-864-6500

- Telephone the NASA STI Information Desk at 757-864-9658

- Write to:
  NASA STI Program
  Mail Stop 148
  NASA Langley Research Center
  Hampton, VA 23681-2199

NASA/TM—2019-220012 AIAA–2018–3492

Independent Effects of Reynolds Number and Mach Number on Aerodynamics of an Iced Swept Wing

Andy P. Broeren
Glenn Research Center, Cleveland, Ohio

Sam Lee
Vantage Partners, LLC, Brook Park, Ohio

Brian S. Woodard
University of Illinois at Urbana-Champaign, Urbana, Illinois

Christopher W. Lum
University of Washington, Seattle, Washington

Timothy G. Smith
Federal Aviation Administration, William J. Hughes Technical Center, Egg Harbor Township, New Jersey

Prepared for the
Aviation Forum
sponsored by the American Institute of Aeronautics and Astronautics
Atlanta, Georgia, June 25–29, 2018

National Aeronautics and
Space Administration

Glenn Research Center
Cleveland, Ohio 44135

July 2019

Acknowledgments

The authors wish to acknowledge the contributions of several key collaborators. Specifically, this work would not have been possible without the unique and outstanding contributions of Mark Potapczuk at NASA Glenn Research Center; Frédéric Moens and Emmanuel Radenac at the Office National d'Etudes et de Recherches Aérospatiales (ONERA); and Mike Bragg, Stephanie Camello, and Kevin Ho at the University of Washington. William Yoshida, an undergraduate student at the University of Illinois, developed and implemented the algorithm to create the contour plots of surface pressure from the individual pressure tap data. Laureline Torz Dupuis, Grégoire d'Ozouville, Grégoire Charpentier, Denis Guérin, and the staff at the ONERA F1 wind tunnel provided exemplary support for the experimental portion of this work. The Federal Aviation Administration and ONERA supported this research through interagency and international agreements, respectively. The NASA-supported portion of this research was originally funded under the Atmospheric Environment Safety Technologies Project of the Aviation Safety Program with continued support under the Advanced Air Transport Technology and Aeronautics Evaluation and Test Capabilities Projects of the Advanced Air Vehicles Program. These individuals, organizations, and projects are gratefully acknowledged.

This work was sponsored by the Advanced Air Vehicle Program
at the NASA Glenn Research Center

Level of Review: This material has been technically reviewed by technical management.

Available from

NASA STI Program
Mail Stop 148
NASA Langley Research Center
Hampton, VA 23681-2199

National Technical Information Service
5285 Port Royal Road
Springfield, VA 22161
703-605-6000

This report is available in electronic form at http://www.sti.nasa.gov/ and http://ntrs.nasa.gov/

Independent Effects of Reynolds Number and Mach Number on Aerodynamics of an Iced Swept Wing

Andy P. Broeren
National Aeronautics and Space Administration
Glenn Research Center
Cleveland, Ohio 44135

Sam Lee
Vantage Partners, LLC
Brook Park, Ohio 44142

Brian S. Woodard
University of Illinois at Urbana-Champaign
Urbana, Illinois 61801

Christopher W. Lum
University of Washington
Seattle, Washington 98195

Timothy G. Smith
Federal Aviation Administration
William J. Hughes Technical Center
Egg Harbor Township, New Jersey 08405

Summary

Aerodynamic assessment of icing effects on swept wings is an important component of a larger effort to improve three-dimensional (3D) icing simulation capabilities. An understanding of ice-shape geometric fidelity and Reynolds and Mach number effects on the iced-wing aerodynamics is needed to guide the development and validation of ice-accretion simulation tools. To this end, wind tunnel testing was carried out for a 13.3-percent-scale semispan wing based upon the Common Research Model airplane configuration. The wind tunnel testing was conducted at the Office National d'Etudes et de Recherches Aérospatiales (ONERA) F1 pressurized wind tunnel with Reynolds numbers of 1.6×10^6 to 11.9×10^6 and Mach numbers of 0.09 to 0.34. Five different configurations were investigated using fully 3D, high-fidelity artificial ice shapes that maintain nearly all of the 3D ice-accretion features documented in prior icing wind tunnel tests. These large, leading-edge ice shapes were nominally based upon airplane holding in icing conditions scenarios. For three of these configurations, lower fidelity simulations were also built and tested. The results presented in this paper show that while Reynolds and Mach number effects are important for quantifying the clean-wing performance, there is very little to no effect for an iced wing with 3D, high-fidelity artificial ice shapes or 3D smooth ice shapes with grit roughness. These conclusions are consistent with the large volume of past research on iced airfoils. However, some differences were also noted for the associated stalling angle of the iced swept wing and for various lower fidelity versions of the leading-edge ice accretion. More research is planned to further investigate the key features of ice-accretion geometry that must be simulated in lower fidelity versions in order to capture the essential aerodynamics.

Nomenclature

Acronyms

CRM	Common Research Model
ESP	electronically scanned pressure
FAA	Federal Aviation Administration
MAC	mean aerodynamic chord
MCCS	maximum combined cross section
NACA	National Advisory Committee for Aeronautics
ONERA	Office National d'Etudes et de Recherches Aérospatiales
RPM	rapid-prototype manufacturing
SLA	stereolithography
WSU	Wichita State University
3D	three-dimensional

Symbols

b	wingspan
c	local streamwise chord length
C_D	drag coefficient
$C_{D,\min}$	minimum drag coefficient
$C_{D,0.6}$	drag coefficient at $C_L = 0.6$
C_L	lift coefficient
$C_{L,\max}$	maximum lift coefficient
$C_{L,\text{use}}$	usable lift coefficient
C_M	quarter mean aerodynamic chord pitching moment coefficient
$C_{M,\min}$	minimum quarter mean aerodynamic chord pitching moment coefficient
C_p	model surface pressure coefficient
M	freestream Mach number
p_o	freestream total pressure
q_∞	freestream dynamic pressure
Re	freestream Reynolds number based on mean aerodynamic chord
$V_{s,1g}$	aircraft 1-g stall speed
x	wing streamwise coordinate
y	wing spanwise coordinate
z	wing thickness coordinate
α	model angle of attack
α_{stall}	stalling angle of attack, consistent with the maximum lift coefficient
α_{use}	usable angle of attack, consistent with the usable lift coefficient

1.0 Introduction

Ice accretion and the resulting aerodynamic effect on large-scale swept wings is an extremely complex problem that affects the design, certification, and safe operation of transport airplanes. Broeren et al. (Ref. 1) describe the current situation, where there is increasing demand to balance tradeoffs in

aircraft efficiency, cost, and noise that tend to compete directly with allowable performance degradations over a large range of icing conditions. These tradeoffs, combined with the ever-present demand to reduce development cost, require an increased reliance on computational tool development. In addition, NASA is conducting research toward future generations of advanced airplane configurations with ambitious goals to improve efficiency while reducing emissions and noise. This research also relies on the development of advanced icing simulation tools in order to realize these design goals. However, sufficient high-quality data to evaluate the performance of these icing simulation tools on iced swept wings are not currently available in the public domain. This problem is being addressed through a large collaborative research effort sponsored by NASA, the Office National d'Etudes et de Recherches Aérospatiales (ONERA), and the Federal Aviation Administration (FAA).

A main objective of this collaborative research effort was accomplished in 2016 with the publication of an experimental ice-accretion database for large-scale swept wings (Ref. 2). A primary purpose of this database is for the evaluation of three-dimensional (3D) icing simulation tools such as those being developed within NASA and ONERA (Refs. 3 and 4). There is an inherent difficulty as to how these comparisons should be conducted because of the large-scale three-dimensionality associated with the experimental ice accretion in some cases (e.g., "scallops" or "lobster tails"). Furthermore, most icing simulation tools are not capable of predicting these large-scale 3D ice features. An important question is how much detail of this 3D geometry is critical to the iced-wing aerodynamics and therefore must be accurately simulated. One possible comparison metric is the resulting potential aerodynamic degradation of the swept wing. Therefore, the remaining objectives of the larger, collaborative research effort are to

- Develop a systematic understanding of the aerodynamic effect of icing on swept wings, including Reynolds and Mach number effects, important flow-field physics, and fundamental differences from iced airfoils.
- Determine the level of ice-shape geometric fidelity required for accurate aerodynamic simulation of swept-wing icing effects.

This paper, along with a series of companion papers (Refs. 5 to 7), provides initial results for these remaining objectives. Additional wind tunnel testing and future publications are planned. The approach used to accomplish these objectives has been successfully carried out in previous icing aerodynamics studies of straight wings and airfoils.

In past work, geometric representations of ice accretion have been attached to wings and models and tested in dry-air wind tunnels or in flight. These geometric representations are referred to as "artificial ice shapes" or "ice-accretion simulations." The various methods and geometric fidelities associated with developing artificial ice shapes have been investigated in a previous NASA and ONERA collaborative research effort named "SUNSET1" (Ref. 8). Since that time, a new approach for producing high-fidelity artificial ice shapes has been developed using 3D scanning and rapid-prototype manufacturing (RPM) (Ref. 9). In past studies of icing performance effects on airfoils, systematic investigations of Reynolds and Mach number effects were conducted (Refs. 10 to 16). Over the course of many years, it was found that aerodynamic tests conducted in the Reynolds number range of 1.0×10^6 to 2.0×10^6 could yield results applicable to flight Reynolds number (e.g., 10×10^6 to 20×10^6) for leading-edge ice shapes. Therefore, the current research effort will determine if similar trends apply for full-span, leading-edge ice on a swept wing. This effort involves both low- and high-Reynolds number aerodynamic testing. The low-Reynolds number aerodynamic testing is being conducted in the Wichita State University (WSU) 7- by 10-ft atmospheric wind tunnel. The high-Reynolds number aerodynamic testing is being conducted in the ONERA F1 11.4- by 14.8-ft pressurized wind tunnel using a larger scale model. The pressurization capability of this facility will allow for independent variations in Reynolds number up to approximately 12×10^6 and Mach number up to approximately 0.34. The results from the ONERA F1 test campaigns will be analyzed for Reynolds and Mach number effects (among other things) and compared with the results of the WSU test campaigns to determine the extent to which iced swept-wing aerodynamic testing can be conducted in smaller scale facilities at lower Reynolds number.

The purpose of this paper is to present the results of the high-Reynolds number testing with the objective of quantifying the effects of Reynolds number and Mach number on clean- and iced-wing performance over the range tested. In order to carry out this objective, aerodynamic testing was conducted at the ONERA F1 wind tunnel using a 13.3-percent-scale semispan wing model of the CRM65. The CRM65 geometry is based upon the Common Research Model (CRM) and is described in previous papers (Refs. 1 and 17 to 20) and in Section 2.2. Clean, tripped, and iced-wing configurations were tested. The artificial ice shapes were based upon 3D scans of ice accretion in the NASA Icing Research Tunnel and fabricated with RPM. The resulting artificial ice shapes were also instrumented to measure surface static pressure. Aerodynamic performance testing was conducted in angle-of-attack sweeps over a Reynolds number range of 1.6×10^6 to 11.9×10^6 and a Mach number range of 0.09 to 0.34. Force balance and surface pressure data were acquired. Mini-tuft flow visualization was also performed during the performance sweeps. The companion papers by Lee et al. (Ref. 5), Woodard et al. (Ref. 6), and Sandhu et al. (Ref. 7) provide more results regarding the effect of artificial ice shapes on the wing aerodynamic performance and flow field.

2.0 Wind Tunnel Facility, Model, and Experimental Methods

2.1 Wind Tunnel Facility

All experiments discussed in this paper were carried out at the ONERA F1 pressurized wind tunnel located at the Fauga-Mauzac Center in southern France. The closed-return tunnel can be pressurized to 56 psi and has a test section approximately 11.5 ft high by 14.8 ft wide (3.5 by 4.5 m). The maximum speed is M = 0.36 at a pressure of approximately 22 psi, which corresponds to a Reynolds number per foot of approximately 3.7×10^6. The maximum Reynolds number is 6.1×10^6/ft at a pressure of approximately 56 psi and M = 0.23. During each experiment, the Mach number was controlled to within ±0.001 while the total pressure and total temperature were controlled to within ±0.03 psi and ±0.4 °F, respectively. The angle-of-attack sweeps were performed with a continuous change in pitch angle at a constant rate of 0.1 deg/sec. The model angle of attack was varied from –6° up to 25° except in cases where dynamic forces limited the maximum angle of attack or a clear local maximum in lift coefficient was measured. Force balance and surface pressure measurements were acquired for most configurations at Reynolds and Mach number combinations shown in Table I along with the approximate values of total pressure (p_o) and dynamic pressure (q_∞). For some configurations, some of these conditions were omitted

TABLE I.—REYNOLDS AND MACH NUMBER CONDITIONS

Reynolds number	Mach number				
	0.09	0.18	0.23	0.27	0.34
1.6×10^6	[a]p_o = 18.9 psi [b]q_∞ = 0.10 psi	----------	----------	----------	----------
2.7×10^6	p_o = 30.5 psi q_∞ = 0.17 psi	p_o = 16.0 psi q_∞ = 0.35 psi	----------	----------	----------
4.0×10^6	p_o = 46.4 psi q_∞ = 0.26 psi	p_o = 23.2 psi q_∞ = 0.52 psi	p_o = 18.9 psi q_∞ = 0.65 psi	p_o = 16.0 psi q_∞ = 0.78 psi	----------
6.8×10^6	----------	p_o = 39.2 psi q_∞ = 0.88 psi	p_o = 31.9 psi q_∞ = 1.1 psi	p_o = 27.6 psi q_∞ = 1.3 psi	p_o = 21.8 psi q_∞ = 1.7 psi
9.6×10^6	----------	p_o = 55.1 psi q_∞ = 1.2 psi	----------	----------	----------
11.9×10^6	----------	----------	p_o = 55.1 psi q_∞ = 2.0 psi	----------	----------

[a]Total pressure.
[b]Dynamic pressure.

in order to optimize the efficiency of the test campaign. The speed control was based upon Mach number, therefore small differences in Reynolds number were observed. For example, the Reynolds number corresponding to M = 0.23 varied between 11.8×10^6 and 12.0×10^6. Torz-Dupuis (Ref. 21) has provided a detailed report of the test setup and instrumentation, data reduction, experimental uncertainties, and wall corrections.

Load measurements were performed using a six-component force balance located beneath the test section floor. This study utilized a reflection plane model, and the force balance was used to measure the lift, drag, and pitching moment. The force balance does not directly measure the lift and drag but rather measures the normal force and the axial force, which are relative to a coordinate system fixed to the force balance. A coordinate transformation is required to determine the lift and drag in the wind axes. The force balance measures the moment about a reference point fixed to the force balance, and it is necessary to transfer the moment to the reference point on the model. For the model used in this study, there was an offset along the x-axis of the force balance between the balance reference point and the model reference point. The model center of rotation and moment center are defined in Section 2.2. In general, the uncertainty of each force balance component was ±0.04 to 0.06 percent of the capacity. The measurement uncertainty in the wing angle of attack was ±0.023°. Specific uncertainty values for the wing forces and pitching moment are described later in this section.

Surface pressure measurements were acquired using miniature electronically scanned pressure (ESP) modules developed by Pressure Systems Incorporated. A total of six 64-channel ESP modules were used, each having a full-scale measurement range of ±15.0 psi. The pressure data acquisition system at F1 is designed to accommodate the changes in tunnel stagnation pressure for the various run conditions through changes in the reference pressure. The system ensures that the fullest range of the ESP modules is utilized without exceeding the measurement limit. Specific uncertainty values for model pressure coefficient are described later in this section. The wind tunnel reference pressures are measured on individual Druck transducers. The resulting uncertainty in the dynamic pressure is an approximately linear function of the magnitude of the dynamic pressure and ranges from ±8.65 percent at the $Re = 1.6\times10^6$, M = 0.09 (lowest dynamic pressure) condition to ±0.46 percent at the $Re = 12.0\times10^6$, M = 0.23 (highest dynamic pressure) condition. This large range of uncertainty in dynamic pressure reflects the challenges of providing instrumentation for a pressurized wind tunnel where there is a correspondingly large range of pressures and forces to be measured.

The uncertainties in the experimental data were determined using the standard root-sum-square method outlined by Coleman and Steele (Ref. 22) and developed by Kline and McClintock (Ref. 23). These uncertainties are estimated for 20:1 odds and use the numerical values for the instrumentation described in the preceding paragraphs. Table II provides a summary of the absolute and relative uncertainties in the model surface pressure coefficient for the lowest and highest dynamic pressure. The uncertainties for other Reynolds and Mach number conditions follows an approximately linear relationship with the corresponding dynamic pressure shown in Table I. The data show that for pressure coefficients of about –5 or less, nearly all of the uncertainty is due to the dynamic pressure itself. For example, the uncertainty in dynamic pressure for $Re = 1.6\times10^6$, M = 0.09 is ±8.65 percent, whereas the uncertainty in the pressure coefficient is ±8.79 percent, meaning 99 percent of the total uncertainty is due to the uncertainty in dynamic pressure. Table III provides a summary of the uncertainties in lift, drag, and pitching moment coefficient for the lowest and highest dynamic pressure for the clean-wing configuration. For the lowest dynamic pressure at $Re = 1.6\times10^6$ and M = 0.09, the uncertainty values are large, especially for the drag and pitching moment coefficients. The large uncertainties reported in Table III are due to low magnitude of the measured force and moment on the force balance. It is important to note that the force balance uncertainties were reported based upon the maximum forces and moments for the current test. Therefore, the total uncertainties reported in Table III would likely be much smaller if the force balance uncertainties were provided over the smaller range associated with the lowest dynamic pressure. In other words, the actual uncertainties in lift, drag, and pitching moment coefficient for the lowest dynamic pressure are likely much lower than the values reported in Table III. Lee et al. (Ref. 5) provide further justification for this conclusion by comparison of the data

TABLE II.—ABSOLUTE AND RELATIVE UNCERTAINTIES IN MODEL SURFACE PRESSURE COEFFICIENT

Reynolds number, Re, Mach number, M	Pressure coefficient	Absolute uncertainty	Relative uncertainty, percent
Re = 1.6×10^6, M = 0.09	±1	±0.116	±11.57
	–5	±0.440	±8.79
Re = 11.9×10^6, M = 0.23	±1	±0.006	±0.62
	–5	±0.023	±0.46

TABLE III.—ABSOLUTE AND RELATIVE UNCERTAINTIES IN FORCE BALANCE DATA

Reynolds number, Re, Mach number, M	Variable	Reference value	Absolute uncertainty	Relative uncertainty, percent
Re = 1.6×10^6, M = 0.09	α[a]	4.99°	±0.023°	±0.46
	C_L[b]	0.5607	±0.0530	±9.45
	C_D[c]	0.0203	±0.0115	±56.78
	C_M[d]	–0.2298	±0.0273	±11.86
Re = 11.9×10^6, M = 0.23	α	4.97°	±0.023°	±0.46
	C_L	0.5951	±0.0038	±0.63
	C_D	0.0186	±0.0007	±3.55
	C_M	–0.2363	±0.0023	±0.96

[a]Model angle of attack.
[b]Lift coefficient.
[c]Drag coefficient.
[d]Quarter mean aerodynamic chord pitching moment coefficient.

acquired on the 8.9-percent-scale model at the WSU wind tunnel. For the highest dynamic pressure at Re = 11.9×10^6, M = 0.23, all of the uncertainty values are much more reasonable and acceptable for the purposes of this work.

The force balance and surface pressure measurements were synchronized in time within the facility data acquisition system. This was important because the data were acquired as the model was pitched continuously at a rate of 0.1 deg/sec. A custom-designed postprocessing routine was written and implemented for these data to conditionally average the results into 0.5° angle-of-attack increments using a ±0.15° window based upon the geometric (uncorrected) angle of attack. For example, data acquired over the interval $3.85° \le \alpha \le 4.15°$ were used to create conditionally averaged values for angle of attack $\alpha = 4°$. In addition to this, the pitching moment coefficient referenced to quarter chord of the mean aerodynamic chord (MAC) was also calculated. In previous reports and papers (Refs. 24 to 26), the pitching moment was referenced to the location described in Section 2.2. After conducting further analysis of the data, a determination was made to report the pitching moment about the quarter chord of the MAC location that is also described in Section 2.2.

All aerodynamic data (α, lift coefficient C_L, quarter MAC pitching moment coefficient C_M, drag coefficient C_D, and model surface pressure coefficient C_p) presented in this paper were corrected for wind tunnel wall effects using a linearized compressible flow method that models the potential flow around the model and the wind tunnel walls. This was an in-house ONERA method that yielded two corrections terms, one of which was constant and the other proportional to the model lift coefficient. The corrections were performed in real time as the data were being acquired; however, the raw data are archived in the event of new postprocessing requirements. In addition to this method, a correction procedure for 3D models outlined in Barlow, Rae, and Pope (Ref. 27) as implemented by WSU (Ref. 28) was also used for comparison. The model and wind tunnel constants used in this method were updated from the WSU-related values to those of the F1 model and wind tunnel. As described in Section 1.0, aerodynamic data acquired at the WSU wind tunnel will be compared with data acquired at the ONERA F1 facility. Therefore, it is important that the effect of the wind tunnel walls on the aerodynamic data from both facilities be accounted for properly. The companion paper by Lee et al. (Ref. 5) provides comparison and analysis of the results of the wall correction schemes. The aerodynamic data reported in this paper were corrected using the ONERA method.

2.2 Wind Tunnel Model Description

The semispan model fabricated for these wind tunnel tests was based on a 13.3-percent-scale version of the CRM65 wing. The full-scale CRM65 geometry has a realistic cruise configuration loading applied to the wing, resulting in a wing shear similar to dihedral (Ref. 17). In order to simplify the design of the removable leading edge segments (described below), this shearing or "bending" of the wing was removed from the model geometry, resulting in an unsheared wing with a straight leading edge across the span of the model. The wing retained the twist and taper of the CRM65. Table IV summarizes the geometric parameters of the wing, and a diagram of the CRM65 planform is shown in Figure 1 with key dimensions. The main body of the model was machined from stainless steel, and the removable leading edge components were machined from aluminum. The model contained 243 pressure taps in its clean configuration. Figure 2 shows photographs of the wing model installed in the wind tunnel with the circular splitter plate. An artificial ice shape is mounted to the leading edge of the wing in these images. Below the circular splitter plate was a streamlined shroud that covered the wing spar. This arrangement isolated the wing spar from any aerodynamic loads. With this arrangement, both the splitter plate and shroud were nonmetric, meaning the aerodynamic forces were only measured on the wing itself. The splitter plate and shroud were designed based upon previous work for the smaller scale WSU wind tunnel model (Refs. 24 and 26).

The model was designed and built with a removable leading edge that allowed artificial ice shapes to be added to the wing. This approach has been used in previous icing aerodynamic studies (Refs. 8, 11, 13, 15, and 16) and allows for very efficient and repeatable changes in the artificial ice-shape configurations. This is important for this research effort, as many different ice-shape configurations were investigated. The three main components of the model were the main element (including a spar that attached to the force balance), a full-span clean leading edge, and a partial-span leading edge used for mounting ice shapes. An open channel exists between the main element and any of the leading-edge components for routing pressure tubing out of the model's base to the data acquisition system. The seam between the clean leading edge and the main element was a straight line on both the upper and lower surfaces, but the seam was not at the same location on both surfaces. Typically, ice accretes farther back on the wing of an aircraft on the lower surface than it does on the upper surface, so the lower surface artificial ice shapes cover a greater portion of the local chord. At the root of the wing, the seam was at 9.3 and 22.9 percent of the local streamwise chord on the upper and lower surfaces, respectively. At the tip of the wing, the seam was at 12.6 and 38.4 percent of the local streamwise chord on the upper and lower surfaces, respectively.

TABLE IV.—SUMMARY OF 13.3-PERCENT-SCALE CRM65 SEMISPAN WING GEOMETRIC PARAMETERS

Span, b, ft (in.)	7.50 (90.00)
Mean aerodynamic chord, MAC, ft (in.)	2.08 (25.01)
Area (geometric), ft^2 (in.^{2})	13.55 (1,951.00)
Volume, ft^3 (in.^{3})	2.09 (3,604.50)
Aspect ratio[a]	8.30
Taper ratio	0.23
Root chord, ft (in.)	3.38 (40.50)
Tip chord, ft (in.)	0.77 (9.28)
Root angle of attack α, deg	4.4
Tip α, deg	–3.8
Quarter-chord sweep angle, deg	35.0
Leading-edge sweep angle, deg	37.2
Location of rotation center[b]	x [c] = 29.05 in., z [d] = 0
Location of moment center[b]	x = 35.80 in., z = 0
Location of 0.25×MAC[b]	x = 26.23 in., z = 0

[a]While the other parameters in this table are defined specifically for this model, the aspect ratio is defined for a complete airplane configuration using the formula $\frac{(2 \times semispan)^2}{2 \times area\ of\ one\ wing}$.

[b](0, 0, 0) is the wing root-section leading edge at zero angle of attack.

[c]x is wing streamwise coordinate.

[d]z is wing thickness coordinate.

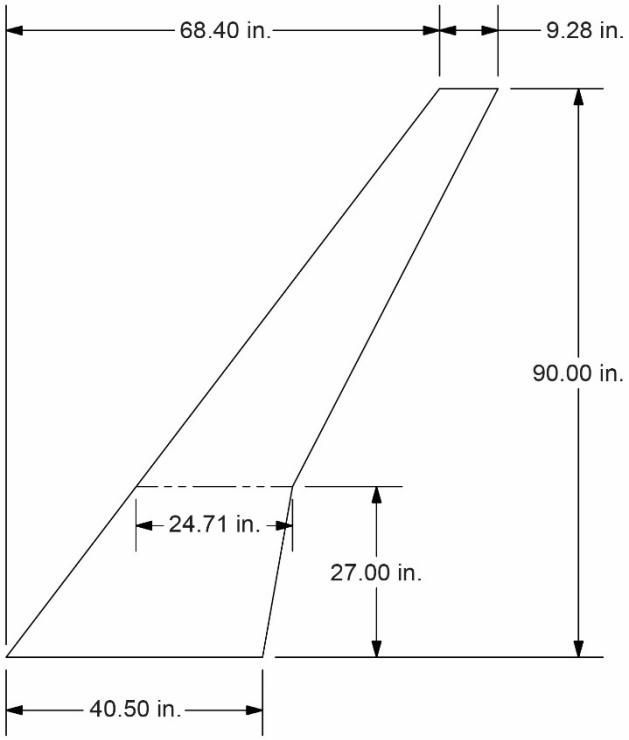

Figure 1.—Semispan wing planform for 13.3-percent-scale CRM65 with key dimensions labeled in inches.

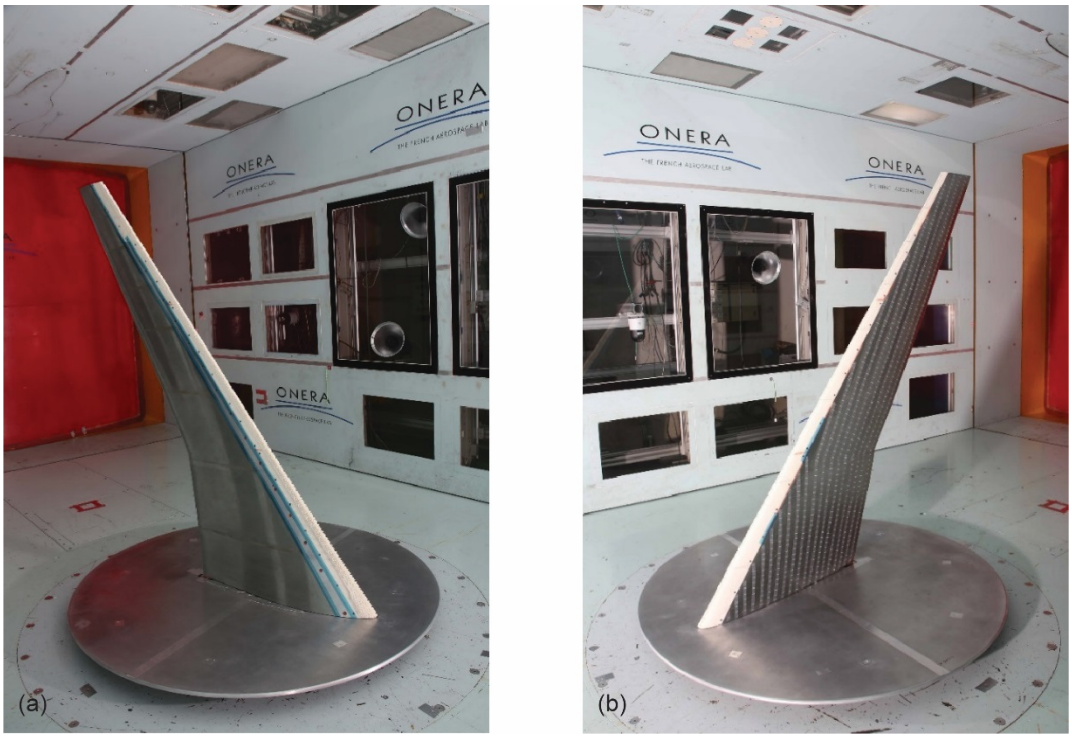

Figure 2.—Installation of 13.3-percent-scale CRM65 semispan wing in ONERA F1 test section. (a) Lower surface of wing. (b) Upper surface of wing.

The partial-span removable leading edge was used to mount the artificial ice shapes to the wing. The partial-span removable leading edge extended from the root to 83.3 percent of the semispan, and it contained a portion of the airfoil contour on the lower surface. Artificial ice shapes were attached to this removable leading edge and covered the entire upper surface. No pressure taps were added to this leading edge. Outboard of this partial-span leading edge, the artificial ice shapes were attached directly to the main element. The reason for this is that the model thickness decreases significantly on the outboard portion of the wing. There was not enough material to extend the removable leading edge. This design does not adversely affect the efficiency or repeatability of the artificial ice-shape configuration changes. The artificial ice shapes were created using an RPM technique called stereolithography (SLA). The SLA process utilizes an ultraviolet laser to solidify liquid polymer resins, and the specific polymer chosen for these components was Accura® 60 (3D Systems, Inc.). Tolerances are advertised to be about ±0.005 in. for this process. A representative ice shape was added to the wing geometry for each segment of wingspan. The leading edge was divided into three segments, each approximately 37.8 in. long. Pressure taps were installed in each of these segments at the same locations as on the clean removable leading edge. The pressure tap holes were included in the RPM design, and then stainless steel tubes were glued into each hole and plumbed to the quick disconnect.

The 243 pressure taps in the model were distributed in seven different streamwise rows. The tap rows were identified by the spanwise location. Further information regarding each of the tap rows can be found in Table V, and the tap row locations are shown graphically in Figure 3. Tap rows 1 through 6 contained upper and lower surface taps as well as a tap located at the leading edge of each row. There were no lower surface taps in row 7 because the wing section was too thin at this location. The taps in the main element of the model were plumbed with stainless steel tubing from their location on the surface and out of the

TABLE V.—PRESSURE TAP INSTRUMENTATION DETAILS

Row identifier	Spanwise location		Taps in RLE[b]	Upper surface	Lower surface	Total taps
	[a]*y/b*	in.				
1	0.111	10.0	20	13	5	38
2	.278	25.0	22	12	4	38
3	.444	40.0	22	12	4	38
4	.600	54.0	22	12	4	38
5	.705	63.5	22	12	4	38
6	.811	73.0	22	12	4	38
7	.900	81.0	7	8	0	15

[a]Normalized spanwise location.
[b]Removable leading edge.

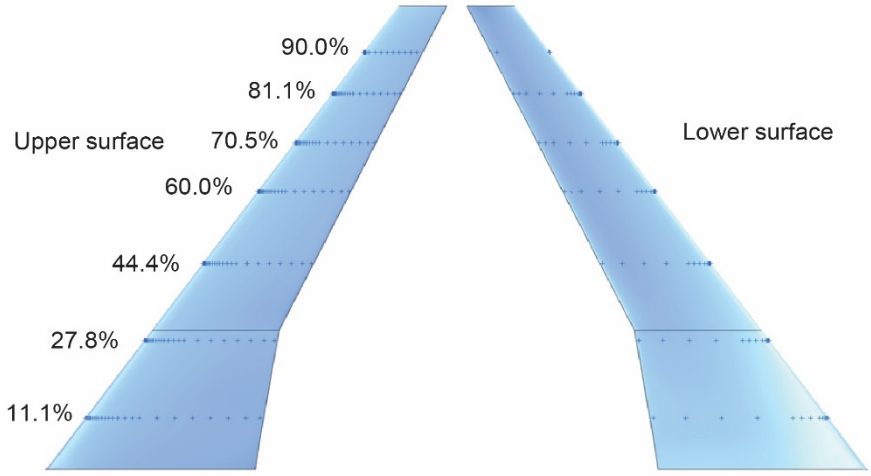

Figure 3.—Pressure tap row locations on wing model.

root of the model. The taps in the leading edge required a more complicated route. The stainless steel tubing in both the clean leading edge and in the RPM ice leading edges transitioned to plastic tubing and then connected to a Scanivalve (Scanivalve Corp.) quick-disconnect fitting. The use of these fittings allowed relatively quick model reconfigurations between clean and RPM leading edges.

2.3 Boundary-Layer Trip Configurations

The model was tested with boundary-layer trips applied near the leading edge on both the upper and lower surfaces of the wing. The trips consisted of CAD Cut (Web Industries, Inc.) trip dots, an off-the-shelf product available in discrete sizes. The trip height was scaled by a factor of 1.5 from the height used in the WSU testing of the 8.9-percent-scale CRM65 wing model, which was based upon the Reynolds number of 1.6×10^6. The resulting trip heights on the F1 model were 0.0031 and 0.0114 in. on the upper and lower surface, respectively. The lower-surface trip location was determined by measuring the surface length from the leading-edge hilite in a direction perpendicular to the leading edge. At tap rows 1, 4, and 6, these distances were 3.00, 2.06, and 1.82 in., respectively. This lower-surface trip location was consistent with the 8.9-percent-scale model. The upper-surface trip was located between 2.5 and 3.0 percent of the local streamwise chord. This location was selected so that the trip was downstream of the leading-edge suction peak for most angles of attack. It should be noted that this location was farther downstream than the location used during the 8.9-percent-scale model tests at WSU. Because this location was different, an additional set of runs was performed with the upper-surface trip located very close to the leading-edge hilite, consistent with the trip configuration on the 8.9-percent-scale model.

2.4 Artificial Ice-Shape Configurations

In addition to the clean aluminum-machined leading edge, several other leading-edge configurations were tested. Numerous artificial ice shapes have been developed for aerodynamic testing and are summarized by Camello et al. (Ref. 25) for the 8.9-percent-scale CRM65 wing tested at WSU. Selected configurations were also tested at F1 on the 13.3-percent-scale model. Table VI provides a summary of these selected configurations and the corresponding nominal icing conditions. Ice-accretion testing was performed on three individual sections of the full-scale CRM65 reference wing: one taken at normalized spanwise location $y/b = 0.20$, called the Inboard model; one taken at $y/b = 0.64$, called the Midspan model; and one taken at $y/b = 0.83$, called the Outboard model. Broeren et al. (Ref. 2) provide more details regarding the ice-accretion testing. The ice shapes were generated based upon an airplane angle of attack of 3.7°. The icing conditions were nominally based upon a CRM65 airplane in holding conditions in the United States Code of Federal Regulations, Title 14, Part 25, Appendix C, Continuous Maximum (hereafter: App. C). The Streamwise/Rime and WB33 ice shapes were directly scaled from App. C to the airspeed of 130 knots. The other conditions were not directly scaled from App. C but instead represent a range in air temperature with the other conditions fixed. The ice-accretion testing was performed in the NASA Icing Research Tunnel, and the ice geometry was measured using the 3D laser scanning method (Ref. 9).

TABLE VI.—SUMMARY OF ICING CONDITIONS FOR F1 TEST CAMPAIGN ARTIFICIAL ICE SHAPES

Ice shape name	Angle of attack, deg	Speed, knots	Total temp., °C	Static temp., °C	MVD[a], μm	LWC[b], g/m^3	Exposure time, min
Maximum Scallop	3.7	130	–6.3	–8.5	25	1.00	29
Small Gap Scallop	3.7	130	–8.7	–11.0	25	1.00	29
Incomplete Scallop	3.7	130	–11.2	–13.5	25	1.00	29
Streamwise/Rime	3.7	130	–17.9	–20.1	25	0.60	23
WB33	3.7	130	–3.1	–5.3	27	0.91	45

[a]Median volumetric diameter.
[b]Liquid water content.

Figure 4 to Figure 8 show photographs of the ice accretion on each of the three models (Inboard, Midspan, and Outboard). The “Maximum Scallop” configuration (Figure 4) was so named because of the well-defined scallop (or “lobster tail”) ice geometry that is clearly shown in the photographs for each model. Decreasing the total temperature 2.4 °C significantly changed the morphology of the scallop geometry as shown in Figure 5. The size, orientation (angle of scallop), and gap between the scallops were all significantly altered, and the ice shape was thus named “Small Gap Scallop.” Decreasing the total temperature another 2.5 °C caused the scallop gaps to close, leaving only some scallop tips at the chordwise extremities of each ice accretion (Figure 6), and the ice shape was thus named “Incomplete Scallop.” The Streamwise/Rime shape shown in Figure 7 was characterized by large-scale rime feathers, particularly on the Inboard model. The ice on the Midspan and Outboard models was characterized by a main ice shape formed at the attachment line with rime feathers downstream. Finally, the WB33 ice shape shown in Figure 8 was characterized by highly 3D ice features, some of which resembled scallop tips. The name “WB33” was derived from the specific flight condition associated with this case (Ref. 2).

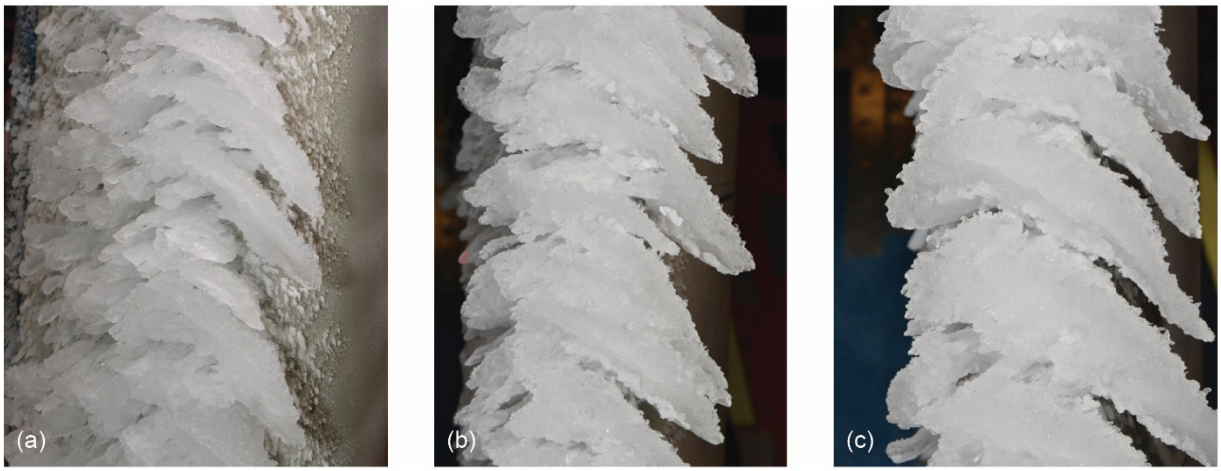

Figure 4.—Maximum Scallop ice shape. (a) Inboard model. (b) Midspan model. (c) Outboard model.

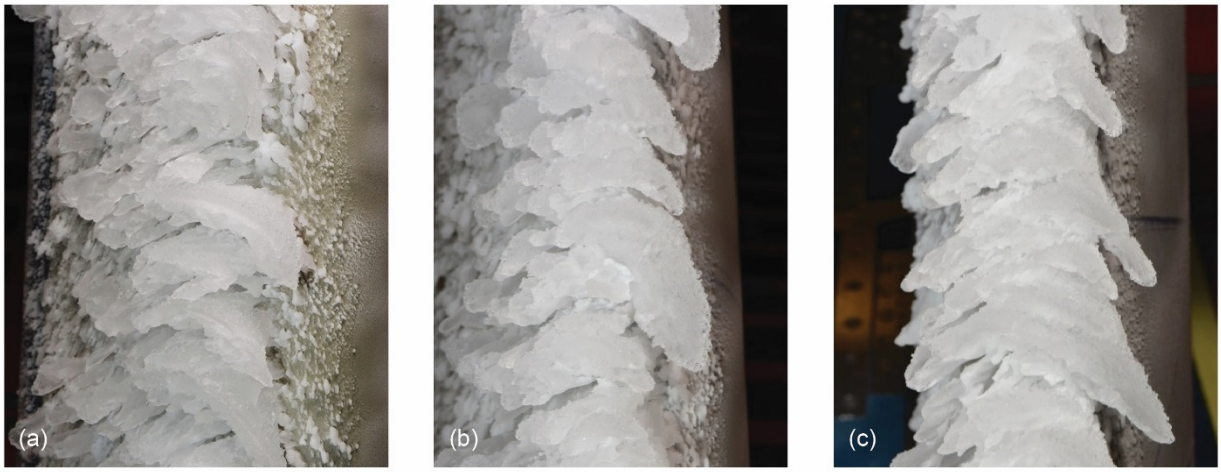

Figure 5.—Small Gap Scallop ice shape. (a) Inboard model. (b) Midspan model. (c) Outboard model.

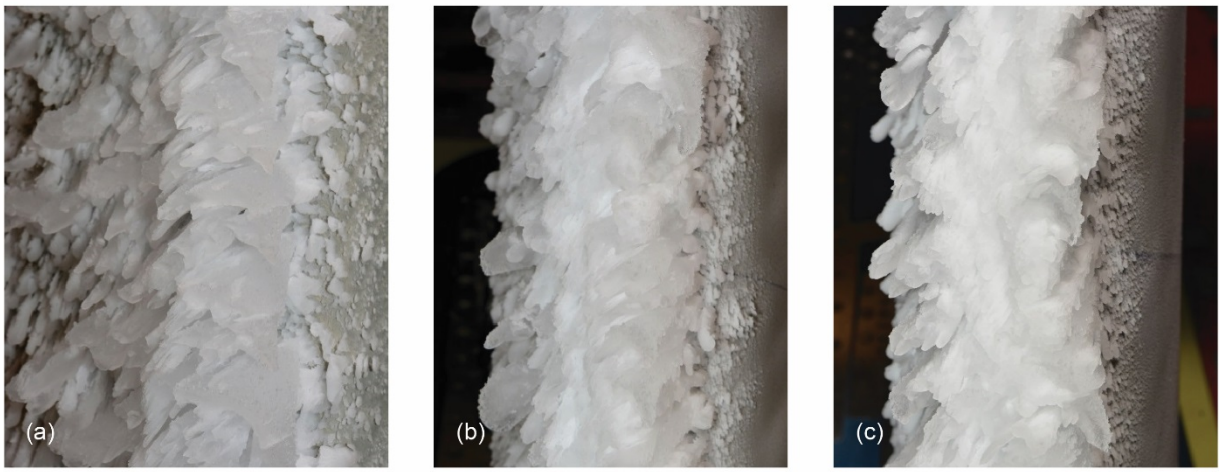

Figure 6.—Incomplete Scallop ice shape. (a) Inboard model. (b) Midspan model. (c) Outboard model.

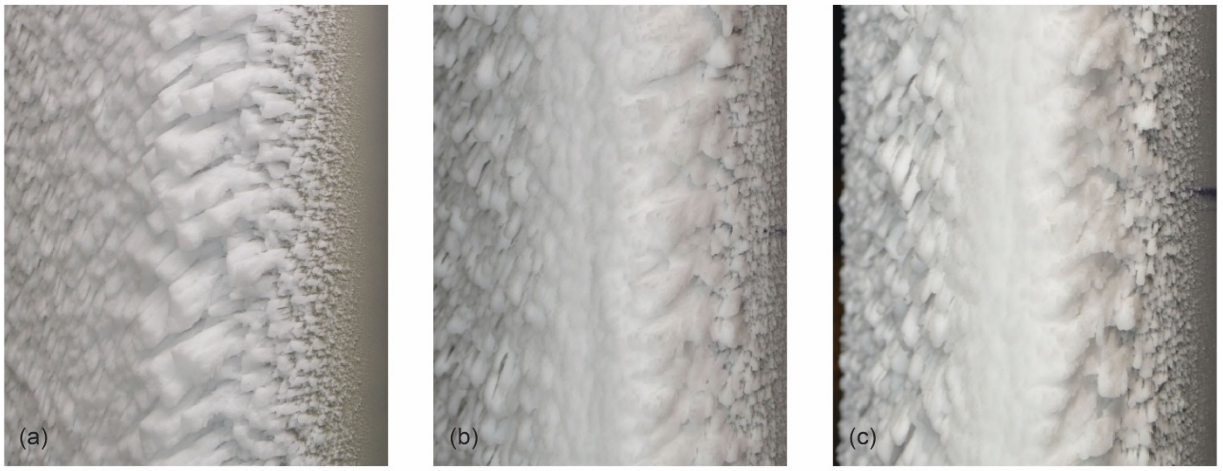

Figure 7.—Streamwise/Rime ice shape. (a) Inboard model. (b) Midspan model. (c) Outboard model.

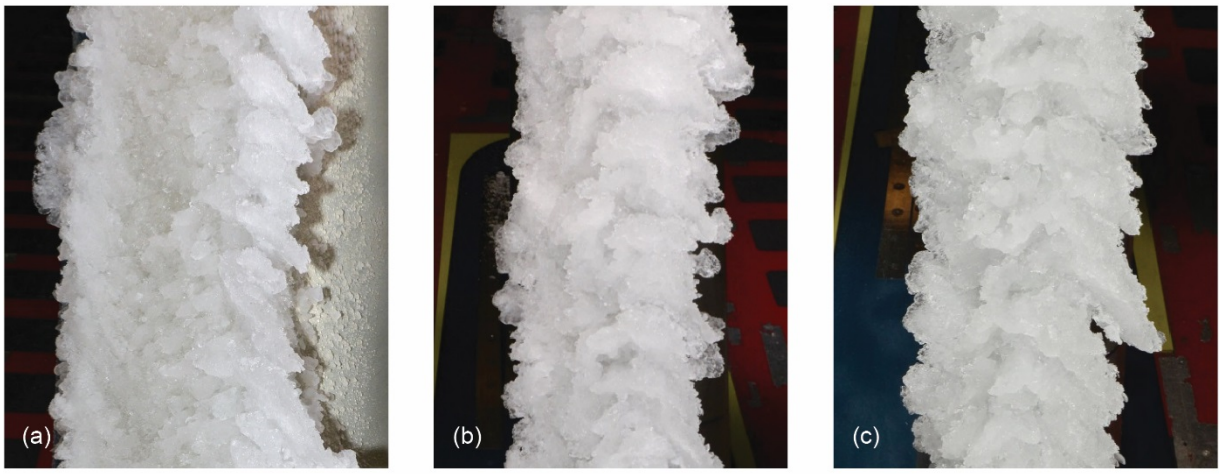

Figure 8.—WB33 ice shape. (a) Inboard model. (b) Midspan model. (c) Outboard model.

Further comparison of these ice geometries is presented in Figure 9 and Figure 10, which show the maximum combined cross section (MCCS) of each ice shape. The MCCS (Ref. 2) was derived from 30 section cuts over a 6-in. spanwise segment of the 3D ice scan. The section cuts were projected onto a single plane and the maximum outer boundary was obtained. The resulting MCCS profile represents the outermost extent of the ice shape over that 6-in. segment. Figure 9 compares the scallop ice formations accreted at different temperatures. The MCCS show some variation in the overall size, but the main differences between these cases are better illustrated in the photographs in Figure 4, Figure 5, and Figure 6. Figure 10 shows the comparison for the Streamwise/Rime and WB33 configurations relative to the Maximum Scallop case for reference. Here there is a much larger variation in the cross section owing to the more significant differences in the icing conditions.

The various 3D ice geometries detailed in this section were used to create full-span artificial ice shapes for aerodynamic testing. Camello et al. (Ref. 29) describe the process used to create the full-span, high-fidelity artificial ice shapes. In this case, "high-fidelity" means that the artificial ice shapes contained nearly all of the 3D features depicted in Figure 4 to Figure 8. Camello et al. (Ref. 29) describe the methodology used to create lower fidelity versions of these ice shapes. Three-dimensional smooth ice shapes were also created from the high-fidelity geometry by taking MCCS-equivalent section cuts along the span, smoothing these cuts and then lofting them into a solid geometry. The 3D smooth ice shapes vary

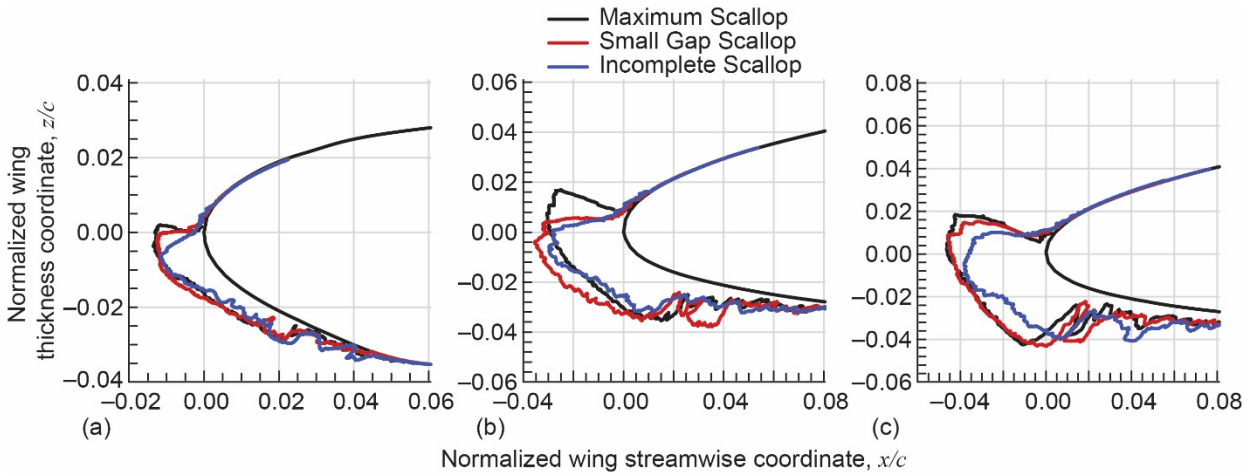

Figure 9.—Comparison of maximum combined cross section for each of the three models for scallop conditions. (a) Inboard model. (b) Midspan model. (c) Outboard model.

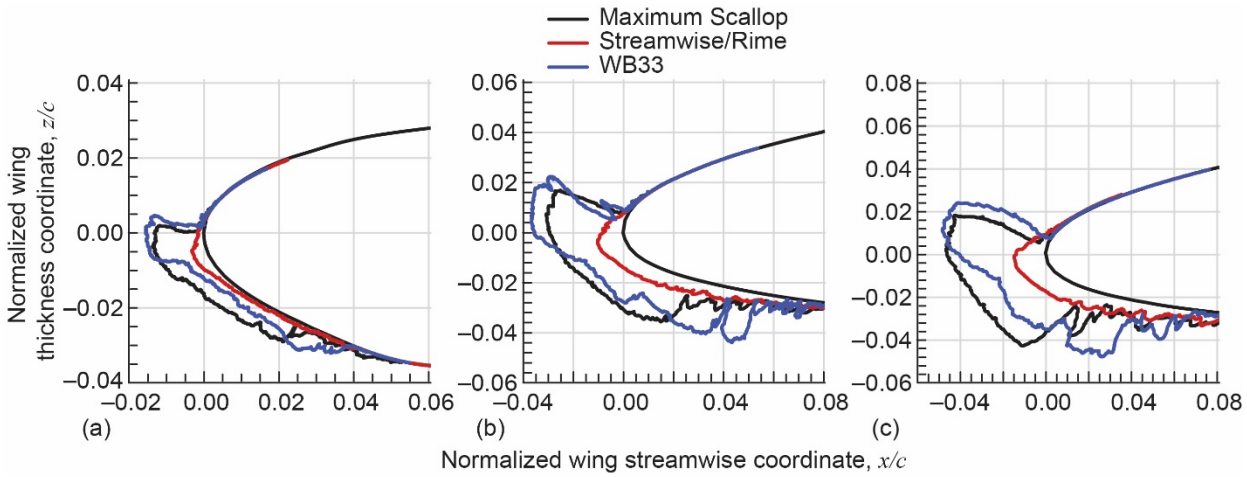

Figure 10.—Comparison of maximum combined cross section for each of the three models for Streamwise/Rime and WB33 ice shapes relative to Maximum Scallop case. (a) Inboard model. (b) Midspan model. (c) Outboard model.

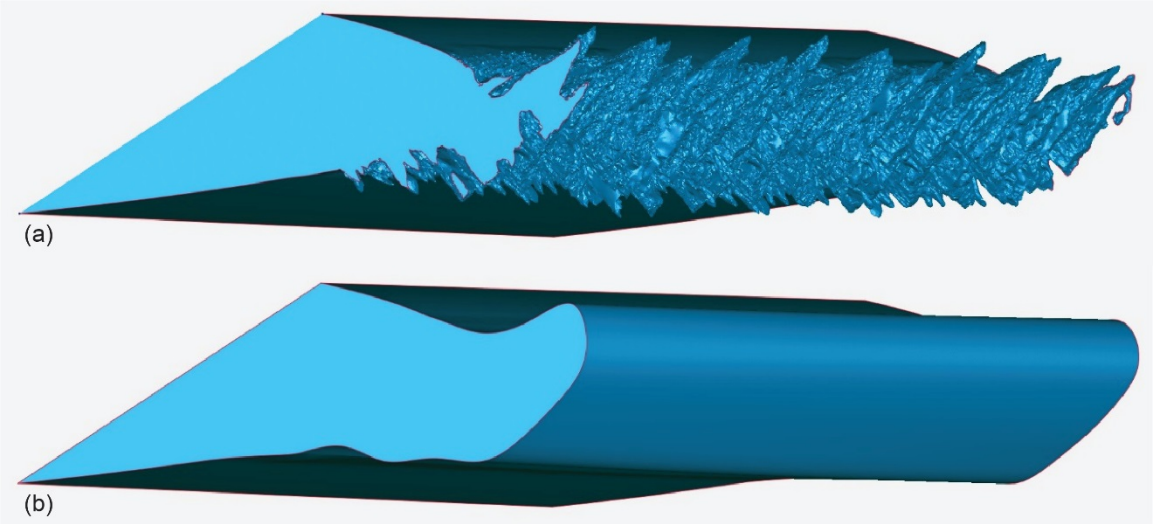

Figure 11.—Comparison of ice-shape geometry. (a) High-fidelity artificial ice-shape geometry. (b) Lower fidelity, 3D smooth geometry.

along the span of the wing, but they do not contain any scallop-type features, feathers, or other ice roughness. A comparison of the high-fidelity and 3D smooth geometries is shown in Figure 11. In some cases, 46-grit silicon carbide grains were glued to the 3D smooth geometry to simulate ice roughness. FAA Advisory Circular 25–25A suggests a height of 3 mm on the full-scale reference geometry. This height is approximately equivalent to 46-grit size on the 13.3-percent-scale model. The grit was applied with full coverage, meaning that all of the surface was entirely covered with the silicon carbide grains. These lower fidelity simulations were designed and built for the Maximum Scallop, Streamwise/Rime, and WB33 ice shapes.

2.5 Flow Visualization

Fluorescent mini-tuft flow visualization was employed during most of the angle-of-attack sweeps performed in this test campaign. The mini-tuft material was 0.006-in.-diameter fluorescent fishing line. The tufts were approximately 1.2 in. long and were applied to the model upper surface using 0.002-in.-thick tape. The general layout of the tufts can be seen in Figure 2(b). Continuous ultraviolent blacklight was used to illuminate the mini-tufts during the angle-of-attack sweeps. The tuft motion was recorded using two high-definition video cameras oriented at different viewing angles. The videos were annotated in real time with the model angle of attack. The tufts were applied to the wing for the tripped and iced-wing configurations. Comparison of force balance data with and without the tufts located downstream of the upper-surface boundary-layer trip showed little to no effect of the tufts on the lift, drag, and pitching moment.

3.0 Results and Discussion

The primary aim of this paper is to report on the effects of Reynolds and Mach numbers on clean-wing and iced-wing aerodynamic performance. A significant portion of this analysis was assigned to defining appropriate performance parameters, such as maximum lift and stall angle. Such parameters allow for analysis of trends in the data. Therefore, this section contains definitions and discussion of these parameters. As an important primer, a brief initial look at the iced-wing aerodynamic performance is presented.

3.1 Effect of 3D, High-Fidelity Artificial Ice Shapes on Wing Performance

As described in Section 2.4, five different 3D, high-fidelity artificial ice-shape configurations were created for this test campaign. The aerodynamic performance effect of these ice shapes on the CRM65 wing is summarized in Figure 12 and Figure 13 at the highest Reynolds number of 11.9×10^6 with M = 0.23. In Figure 12, the main variation in artificial ice-shape geometry was the level of three-dimensionality associated with the degree of scallop formation. The Maximum Scallop configuration, with the most clearly defined scallop formations, resulted in the highest drag and lowest maximum lift.

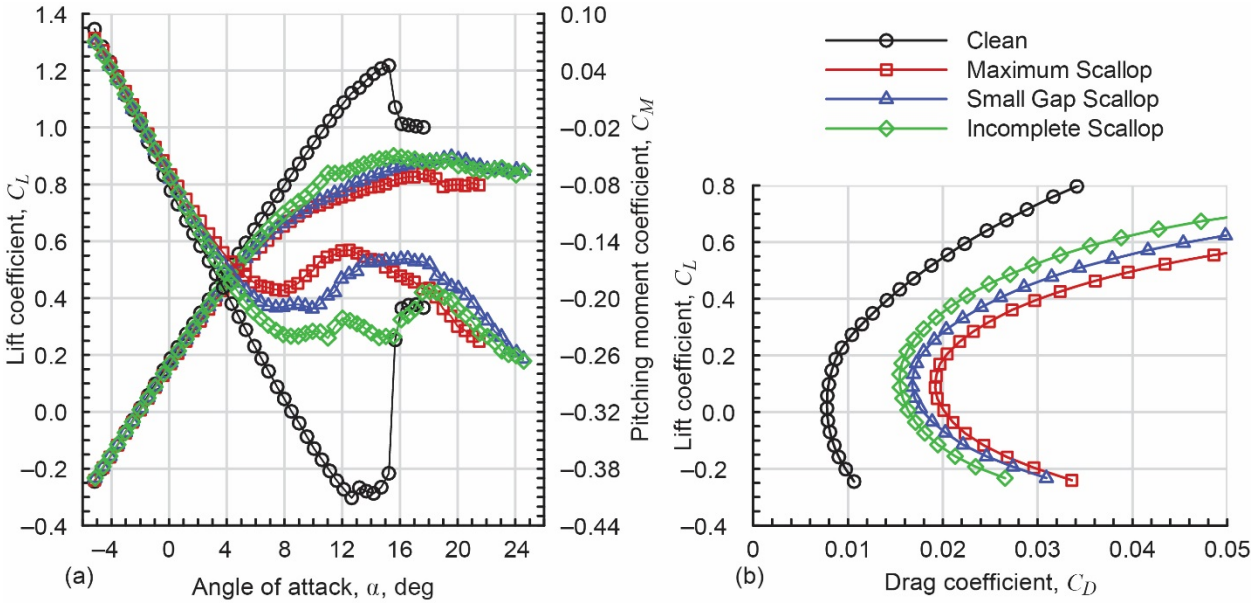

Figure 12.—Comparison of iced-wing performance effects for 3D, high-fidelity Maximum Scallop, Small Gap Scallop, and Incomplete Scallop artificial ice shapes at Reynolds number Re = 11.9×10^6 and Mach number M = 0.23. (a) Effect on lift and pitching moment coefficient. (b) Effect on drag coefficient.

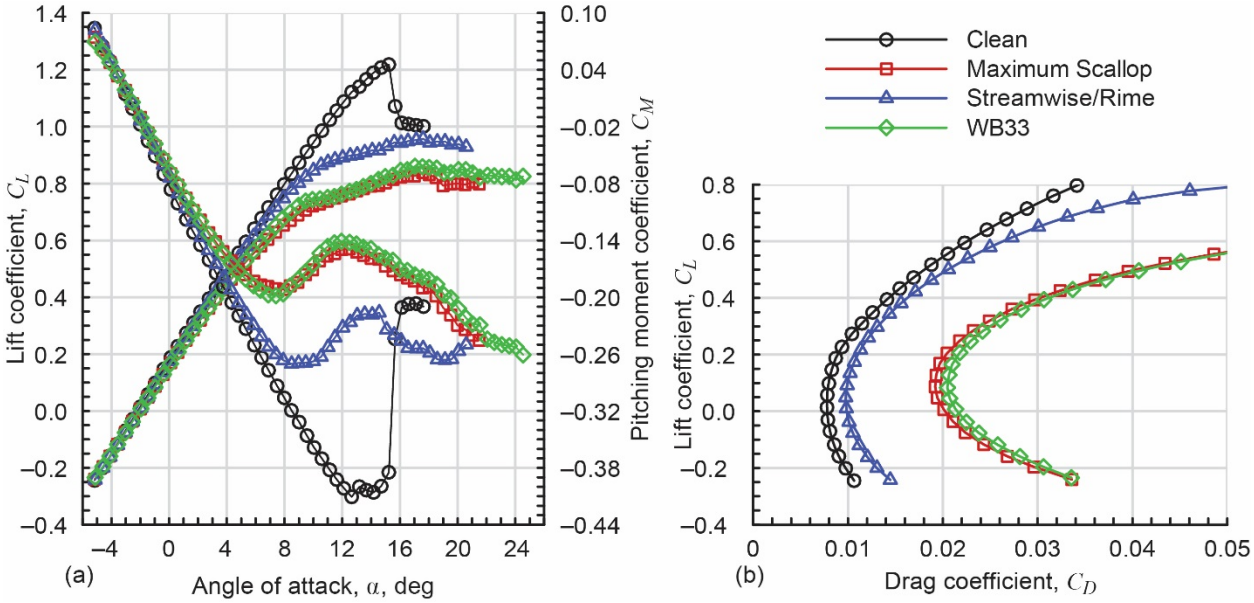

Figure 13.—Comparison of iced-wing performance effects for 3D, high-fidelity Maximum Scallop, Streamwise/Rime, and WB33 artificial ice shapes at Reynolds number Re = 11.9×10^6 and Mach number M = 0.23. (a) Effect on lift and pitching moment coefficient. (b) Effect on drag coefficient.

The drag was clearly lower and maximum lift was clearly higher for the Small Gap and Incomplete Scallop configurations, where the scallop features were less well defined and generally smaller. These results show the effect of varying scallop features on wing aerodynamic performance. Figure 13 shows the effect on aerodynamic performance from the two remaining high-fidelity artificial ice-shape configurations. The Maximum Scallop configuration is also plotted as a point of reference back to Figure 12. These results show that the adverse aerodynamic effect of a streamwise or rime ice configuration was significantly less than that of the other configurations, consistent with its smaller overall thickness and 3D variation. In contrast, the WB33 configuration resulted in deleterious aerodynamic effects that were very similar to the Maximum Scallop configuration. This is significant because the WB33 configuration was based upon App. C airplane certification conditions, whereas the Maximum Scallop configuration was not.

The lift coefficient, C_L, plotted against angle of attack α in Figure 12 and Figure 13 for the wing with artificial ice shapes, was characterized by some common features relative to the clean-wing configuration. These lift curve characteristics were related to changes in the pitching moment, C_M, which is also plotted against angle of attack α for direct comparison. For the iced-wing configuration, the lift curve slope begins to decrease significantly in the same angle-of-attack range where the pitching moment reaches the first local minimum. For example, consider the Maximum Scallop configuration for angles of attack between 6° and 8° where C_M approaches a local minimum and the lift curve indicates a significant departure from the clean configuration. The data show that C_L continues to increase for the iced-wing configurations up to relatively high angles of attack. These characteristics associated with the iced-wing lift curves in the stall regions prompted analysis designed to clearly identify a set of performance metrics used to summarize the large data set from this test campaign. This analysis is described in the next section.

3.2 Definition of Aerodynamic Performance Parameters

3.2.1 Lift-Based Parameters

Iced aerodynamics has traditionally focused on maximum lift coefficient and the corresponding angle of attack as the most significant and easily identifiable performance parameters. Maximum lift coefficient is defined as the first local maximum in the lift curve, with the corresponding angle of attack designated as the stall angle. Using the clean configuration as an example, $C_{L,\max} = 1.22$ at $\alpha_{stall} = 15.2°$ (cf. Figure 12). For the iced-wing configurations shown in Figure 12 and Figure 13, the maximum lift coefficients are fairly well defined by a local maximum. However, these $C_{L,\max}$ values are associated with stall angles that are larger than for the clean wing. The iced-wing configurations shown in Figure 12 have stall angles ranging from 15.6° to 19.6°. In many other cases, the corresponding stall angles were also higher than the clean-wing value, as high as $\alpha_{stall} = 22.7°$. This represents a fundamental difference from past research on straight wings or airfoils with large, leading-edge artificial ice shapes where the stall angle was lower than the clean value. The lift curves for some configurations acquired at different Reynolds and Mach number conditions exhibited poorly defined local maxima where there was more of a “plateau” in the lift curve instead of a well-defined “peak.” Therefore, the use of maximum lift coefficient and stalling angle may not necessarily be indicative of the stall progression on the swept CRM65 wing with artificial ice shapes. The large reduction of lift-curve slope shown for the iced-wing configurations in Figure 12 and Figure 13 indicates significant flow separation. This separation occurs on the outboard portions of the wing and is represented in Figure 12 and Figure 13 by the changes in the pitching moment curve. The outboard flow separation has also been determined through analysis of the flow visualization and surface pressure distributions to be presented later in this section. These observations led to the identification of an additional performance metric that was associated with the change in the pitching moment coefficient.

In 1957, Furlong and McHugh published a National Advisory Committee for Aeronautics (NACA) technical report summarizing the low-speed aerodynamic characteristics of swept wings based upon all known data collected through August 15, 1951 (Ref. 30). Furlong and McHugh identified a performance-based parameter termed “usable” lift or “inflection” lift based upon their review of previous work. For

convenience, the authors assumed that the quarter MAC location was coincident with the airplane center of gravity. Therefore, the longitudinal stability could be referred to as either "stable" or "unstable" depending upon the slope of the pitching moment curve with respect to angle of attack. The change from a negative slope to a positive slope thus indicated a change from a longitudinally stable situation to a longitudinally unstable one. The term "inflection lift" refers to the local minimum in the C_M versus α curve representing the change in slope. The authors also clarified that the term "usable lift coefficient" represents the lift coefficient beyond which stall control is required. This interpretation of usable lift implies that a certain amount of flow separation on the wing has crossed some threshold such that this value of the usable lift coefficient may be more significant than the absolute value of the maximum lift coefficient. This interpretation of usable lift is applicable to the iced-wing aerodynamic effects observed within the present data set.

The 3D, high-fidelity Maximum Scallop configuration can be used as an example to further illustrate the usable lift coefficient, $C_{L,\text{use}}$, as a meaningful performance metric. As shown in Figure 12, the first local minimum in C_M ($C_{M,\text{min}} = -0.19$) occurred at usable angle of attack $\alpha_{\text{use}} = 7.9°$ and $C_{L,\text{use}} = 0.77$. The corresponding distribution of wing upper-surface pressure is shown in Figure 14. These contours were based upon a linear interpolation of the discrete pressure-tap data. The pressure taps used for the interpolation are shown on these plots as small open circles. Owing to this interpolation, any local flow effects that might have occurred between the pressure taps' rows will not be revealed in these contours. Instead, the contours provide an overall look at the upper-surface pressure distribution. With this description in mind, the pressure contours for $\alpha = 7.9°$ in Figure 14 show that the flow over the wing was well behaved, with fairly uniform streamwise and spanwise variations in surface pressure. This picture is contrasted with the contour for $\alpha = 9.9°$, where there was a large redistribution of pressure. The chordwise and spanwise uniformity no longer existed at this angle of attack. The pressure contours indicate likely flow separation outboard of pressure row 4 ($y = 54.0$ in.; $y/b = 0.6$). While the coefficient of lift continued to increase with angle of attack up to 17.6°, the regions of separated flow also continued to increase in size. Thus, the identified usable lift coefficient ($C_{L,\text{use}} = 0.77$ at $\alpha_{\text{use}} = 7.9°$) provides an indication of the lift coefficient that can be attained in this configuration before significant flow separation develops over the wing.

This example illustrates how the concept of usable lift can be employed to describe where the wing begins to stall in a way that is consistent with the original definition proposed by Furlong and McHugh (Ref. 30). It is important to note that the inflection point, or first local minimum, in the pitching moment that defines $C_{L,\text{use}}$ is not always well defined. As an example, consider the Small Gap Scallop configuration in Figure 12. The C_M curve tends to flatten out in the region of the first local minimum at $\alpha = 7.4°$, which is

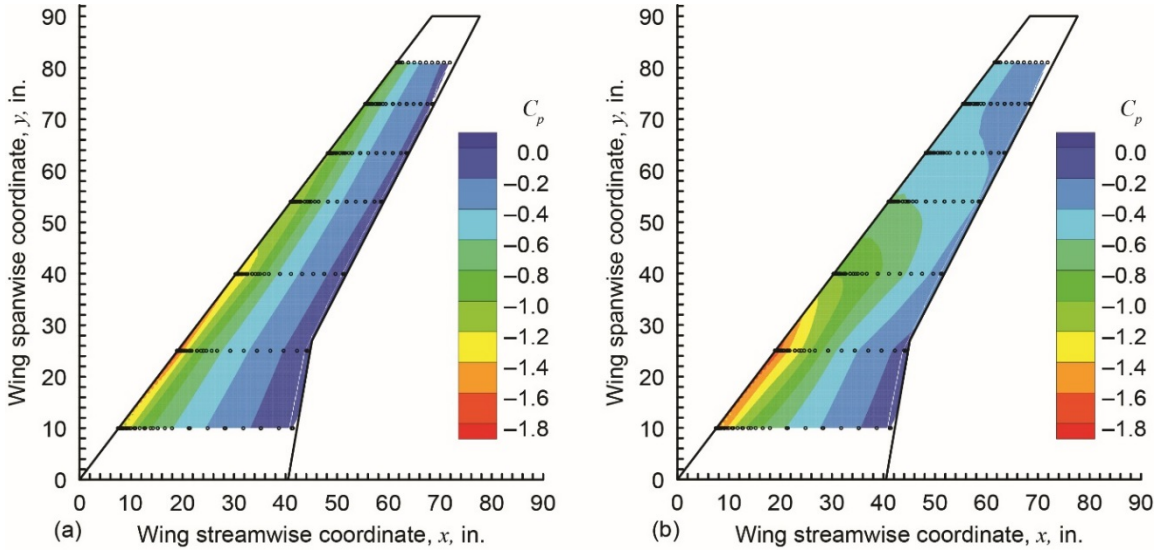

Figure 14.—Contours of upper-surface pressure coefficient C_p for 3D, high-fidelity Maximum Scallop configuration at Reynolds number Re = 11.9×10^6 and Mach number M = 0.23. (a) For angle of attack $\alpha = 7.9°$. (b) For $\alpha = 9.9°$.

followed by a second minimum at $\alpha = 9.9°$. For this configuration, the change in stall progression over these angles of attack was not as significant as that illustrated in the previous paragraph for the Maximum Scallop configuration. This type of ambiguity in the usable lift coefficient is analogous to the situation in defining the maximum lift coefficient, where the lift curve tends to reach a plateau rather than having a well-defined local maximum. Therefore, the information provided by $C_{L,\text{use}}$ and $C_{L,\text{max}}$ can be taken together as complementary performance-based parameters.

3.2.2 Drag-Based Parameters

The artificial ice-shape configurations developed for aerodynamic testing were partly based upon typical airplane holding scenarios in App. C conditions. As a result, the leading-edge ice shapes were large, as shown in Section 2.4. In 2001, Lynch and Khodadoust published "a systematic and comprehensive review, correlation, and assessment of test results available in the public domain which address the aerodynamic performance and control degradations caused by various types of ice accretions on the lifting surfaces of fixed wing aircraft" (Ref. 31). The authors directly address the importance of drag penalties due to leading-edge ice accretion, stating that such penalties are a concern because they can lead to reductions in aircraft climb and acceleration gradients, range, and speed. Lynch and Khodadoust point out that accidents and incidents have been reported with autopilots not augmented with autothrottle during icing exposure where the airspeed can be reduced to stall entry without warning. In addition to these practical considerations, it is important from a research perspective to understand how the drag coefficient may be affected by changes in Reynolds number and Mach number.

Lynch and Khodadoust (Ref. 31) suggest two conditions for the assessment of icing-related drag penalties. The first condition is simply the value of the minimum drag coefficient ($C_{D,\text{min}}$). For the clean-wing and iced-wing configurations in this paper, the minimum drag coefficient is always near zero lift because of the influence of induced drag for nonzero lift coefficients. The other condition that Lynch and Khodadoust recommend is that corresponding to a flight speed 30 percent above the 1-g stall speed ($V_{s,1g}$) for the clean reference geometry. This is equivalent to a lift coefficient that is 59 percent of $C_{L,\text{max}}$ for the clean wing. As discussed later in Section 3.3, there is a significant dependence of the clean-wing $C_{L,\text{max}}$ upon Reynolds and Mach numbers, with values ranging from 0.98 to 1.23. In order to simplify the analysis of iced-wing drag penalties, a reference value of $C_L = 0.6$ was selected, which corresponds to a $C_{L,\text{max}} = 1.014$ for a speed of 1.3 $V_{s,1g}$. The reference value of $C_L = 0.6$ was also selected because it is lower than all of the values of $C_{L,\text{use}}$ identified for these iced-wing configurations. This means that the drag penalties associated with this lift coefficient are still within the range of lift coefficient prior to the onset of significant stall progression on the wing. All of the drag-polar data were analyzed to determine the minimum drag coefficient and the drag coefficient at $C_L = 0.6$ ($C_{D,0.6}$).

3.3 Clean-Wing Reynolds and Mach Number Results

The pressurization capability of the F1 wind tunnel was fully exploited to investigate the independent effects of Reynolds and Mach numbers on the 13.3-percent-scale wing aerodynamics. As shown in Table I, the effect of Reynolds number was measured at constant Mach numbers of 0.09, 0.18, 0.23, and 0.27. Figure 15 shows a comparison of lift, drag, and pitching moment for the M = 0.09 conditions. Readily observable is the significant increase in $C_{L,\text{max}}$ and α_{stall} over this range of Reynolds number. As the Reynolds number was increased from 1.6×10^6 to 4.0×10^6, maximum lift coefficient increased approximately 20 percent from 0.98 to 1.19 while stall angle increased 3.6° from 12.6° to 16.2°. The data illustrate the behavior of $C_{L,\text{use}}$ as identified by the minimum C_M. For $\text{Re} = 1.6\times10^6$, the value of $C_{L,\text{use}}$ was 0.95, which was very close to the value of $C_{L,\text{max}} = 0.98$. As Reynolds number was increased, the minimum C_M occurred at approximately the same angle of attack while the lift coefficient continued to increase to stall. There was, however, a noticeable reduction in the lift-curve slope that approximately corresponded to $C_{M,\text{min}}$. The drag polar plotted in Figure 15 indicates a reduction in the minimum drag coefficient of 11 drag counts ($\Delta C_{D,\text{min}} = 0.0011$) over this range of Reynolds number. There was also a reduction in drag coefficient at $C_L = 0.6$ of 13 drag counts ($\Delta C_{D,0.6} = 0.0013$).

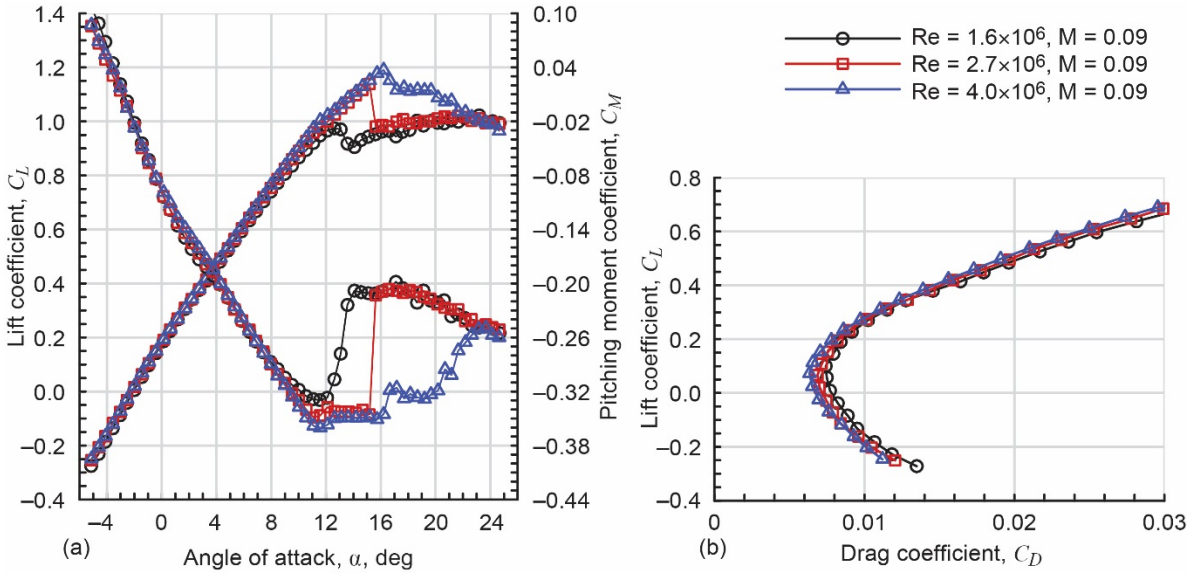

Figure 15.—Effect of Reynolds number Re on clean-wing performance at Mach number M = 0.09. (a) Effect on lift and pitching moment coefficient. (b) Effect on drag coefficient.

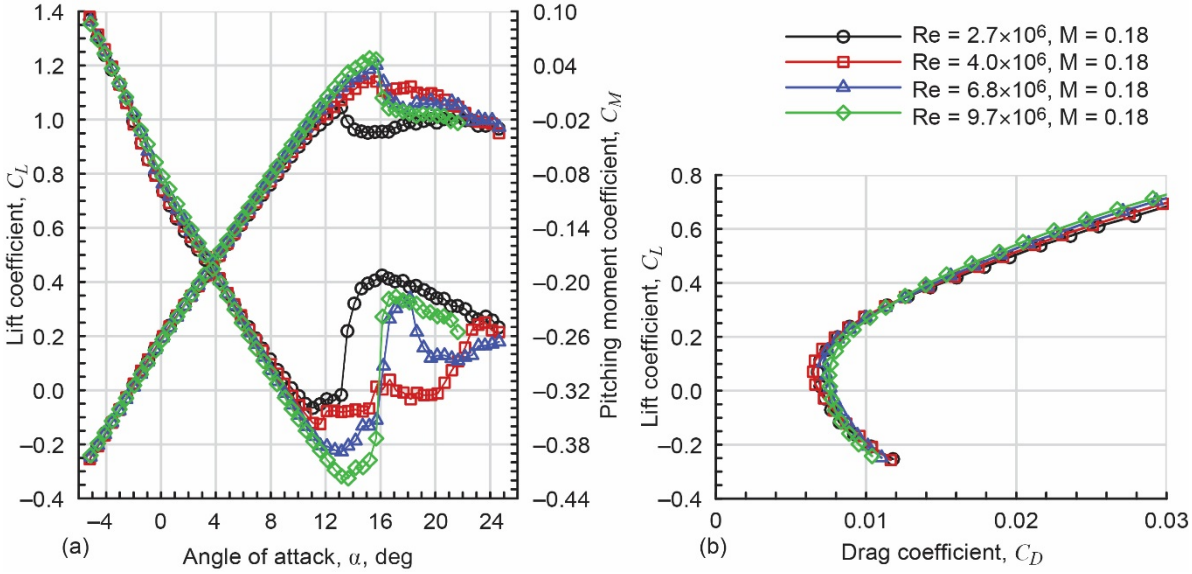

Figure 16.—Effect of Reynolds number Re on clean-wing performance at Mach number M = 0.18. (a) Effect on lift and pitching moment coefficient. (b) Effect on drag coefficient.

Similar significant changes in the wing performance characteristics were also observed as the Reynolds number was increased to 9.7×10^6 at M = 0.18, as illustrated in Figure 16. Maximum lift coefficient was again increased by approximately 20 percent from 1.04 at Re = 2.7×10^6 to 1.23 at Re = 9.7×10^6, with a corresponding increase in stall angle from 13.1° to 15.2°. The minimum in C_M was coincident with a distinct reduction in the lift-curve slope, while C_L continued to increase toward stall. There was a reversal in the trend with respect to the minimum drag coefficient. For these data, the lowest value of $C_{D,\min}$ was measured at Re = 4.0×10^6, with $C_{D,\min}$ increasing at the two higher Reynolds numbers. At $C_L = 0.6$, the drag coefficient was lowest for Re = 9.6×10^6 with a value of 0.0228 and increased to 0.0250 at Re = 2.7×10^6. Reynolds number was further increased to Re = 11.9×10^6 at M = 0.23. Data on the clean wing for this condition were presented in Figure 12 and Figure 13, and the Reynolds number trends at M = 0.23 were similar to those shown in Figure 16.

As shown in Table I, the effect of Mach number was measured at constant Reynolds numbers of 2.7×10^6, 4.0×10^6, and 6.8×10^6. Figure 17 shows a comparison of lift, drag, and pitching moment for the $Re = 6.8\times10^6$ conditions. The largest effect of Mach number was observed in the maximum lift coefficient and stall angle. As the Mach number was increased from 0.18 to 0.34, maximum lift coefficient decreased approximately 20 percent from 1.20 to 1.01, while the stalling angle decreased 3.6° from 15.7° to 12.1°. There was a change in the stalling characteristics at M = 0.34, where the lift coefficient did not decrease significantly as the angle of attack was increased past $C_{L,\max}$. Also for the M = 0.34 condition, the value of $C_{L,\text{use}} = 0.97$ was close to $C_{L,\max}$, while there was a much larger difference between these values for the lower Mach numbers. As indicated in Figure 17, there was very little measureable change in the drag coefficient or pitching moment coefficient outside of the stall region. Very similar trends were observed for the Mach number variation at a constant Reynolds number of 2.7×10^6 and 4.0×10^6.

The maximum lift coefficient and usable lift coefficients were extracted from the performance data and are plotted as a function of Reynolds number in Figure 18. Clearly shown is the trend of increasing $C_{L,\max}$ and $C_{L,\text{use}}$ with increasing Reynolds number. These variations were nonlinear, with most of the increases in $C_{L,\max}$ and $C_{L,\text{use}}$ occurring for Reynolds numbers less than 6.0×10^6. These curves do suggest, however, that the maximum lift coefficient for the clean wing may still continue to increase for Reynolds numbers greater than 12.0×10^6. The variation in $C_{L,\max}$ with Reynolds number is generally consistent with a significant amount of airfoil section data compiled by Broeren et al. (Ref. 16), where the largest increases were observed for Reynolds numbers less than 6.0×10^6. Data were reported for NACA 23012, NACA 0012, GLC–305, and NLF–0414 airfoils for Reynolds numbers up to 16.0×10^6 and M = 0.20. Experimental data for swept wings are more challenging to compare because of the inherent dependence upon the wing configuration, such as sweep angle, aspect ratio, twist, taper, and other parameters. Koven and Graham (Ref. 32) documented the performance of an aspect-ratio-6 wing having a 37° leading-edge sweep angle that was comparable to the 13.3-percent-scale CRM65 wing in the present study. Tests were conducted at the Langley 19-foot pressure tunnel, where the Reynolds number was varied from 2.0×10^6 to 9.4×10^6 with corresponding Mach number variation from 0.08 to 0.18. Consistent with the present data, $C_{L,\max}$ increased from approximately 0.98 at $Re = 2.0\times10^6$ and M = 0.08 to 1.27 at $Re = 6.8\times10^6$ and M = 0.13, with no further increase as Reynolds and Mach numbers increased.

The data in Figure 18 also show that Mach number had the opposite effect, where $C_{L,\max}$ and $C_{L,\text{use}}$ decreased with increasing Mach number. This effect is summarized better in Figure 19 for each of the Reynolds number conditions. The data indicate that the maximum lift coefficient could decrease with

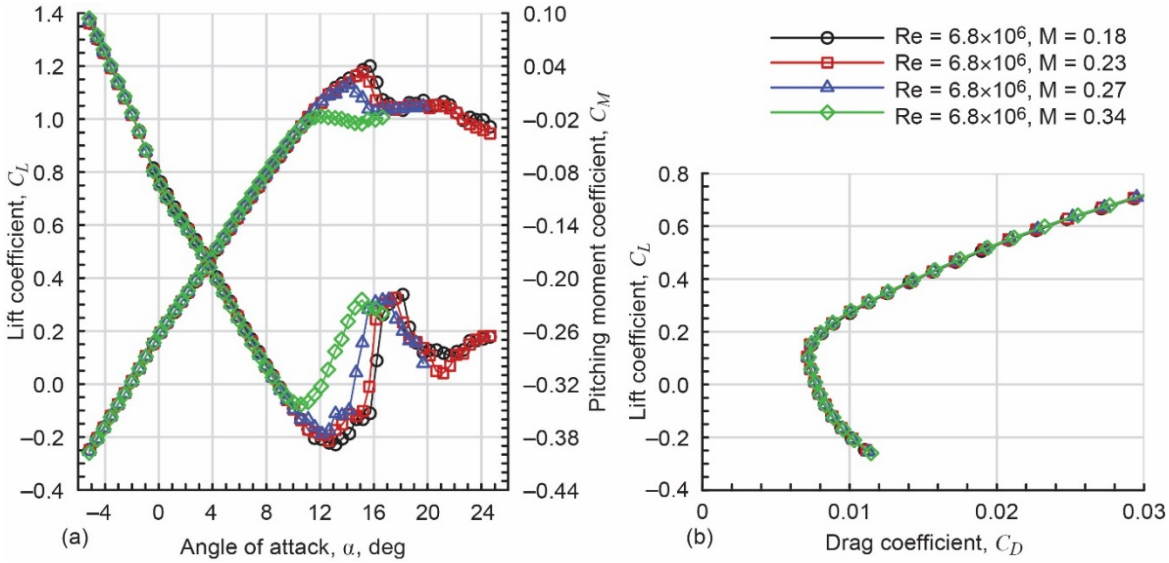

Figure 17.—Effect of Mach number M on clean-wing performance at Reynolds number $Re = 6.8\times10^6$. (a) Effect on lift and pitching moment coefficient. (b) Effect on drag coefficient.

further increases in Mach number greater than 0.34. However, usable lift coefficient approached a near-constant value for M > 0.27. The trend observed in $C_{L,\max}$ was again consistent with the large volume of airfoil data presented in Broeren et al. (Ref. 16), with the decreasing values persisting for M > 0.34. As noted in the previous paragraph, finding comparable swept-wing data is challenging. In one report, Edwards and Boltz (Ref. 33) documented the aerodynamics of an aspect-ratio-6 wing having a 37.25° leading-edge sweep angle for Mach number variations from 0.18 to 0.94 at a constant Reynolds number of 2.0×10^6. This wing exhibited a decrease in $C_{L,\max}$ from approximately 1.01 to 0.90 as Mach number was increased from 0.18 to 0.40. Unfortunately, the authors did not report $C_{L,\max}$ values for larger Mach numbers, nor did they provide any explanation.

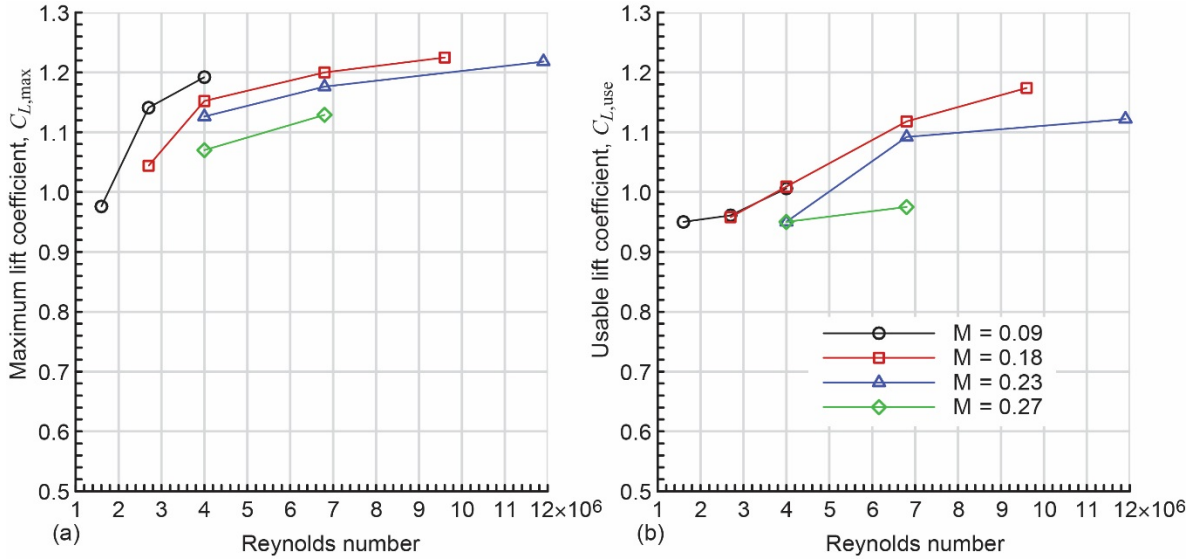

Figure 18.—Effect of Reynolds number on lift coefficients for clean wing at various Mach numbers M. (a) Effect on maximum lift coefficient. (b) Effect on usable lift coefficient.

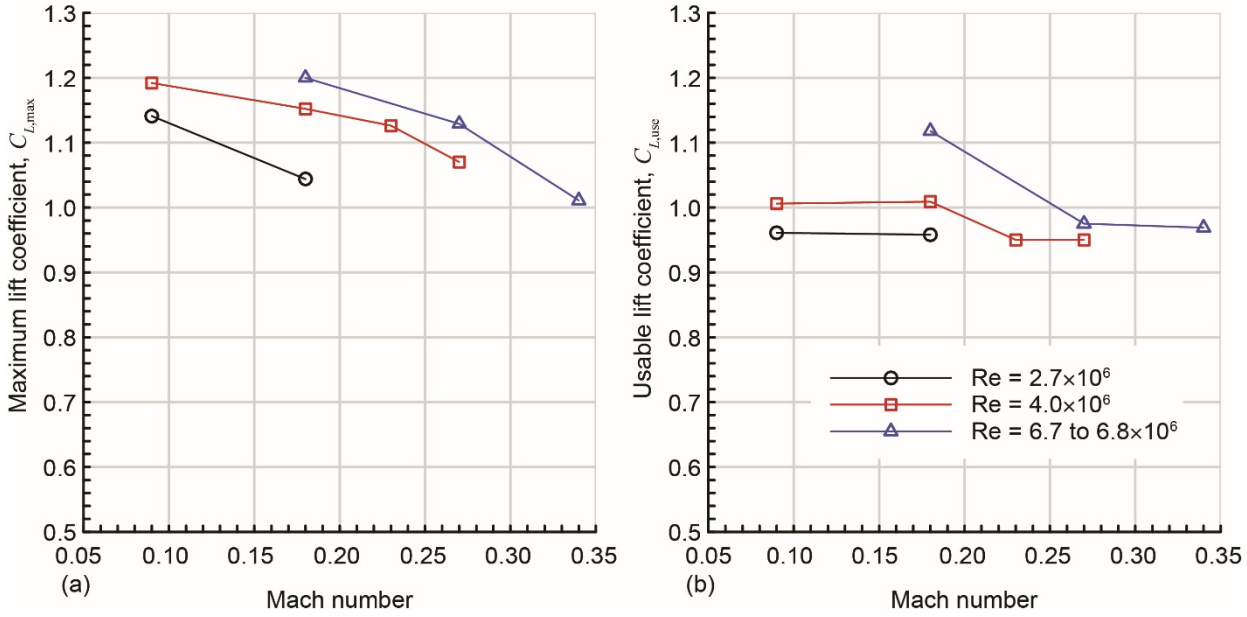

Figure 19.—Effect of Mach number on lift coefficients for clean wing for various Reynolds numbers. (a) Effect on maximum lift coefficient. (b) Effect on usable lift coefficient.

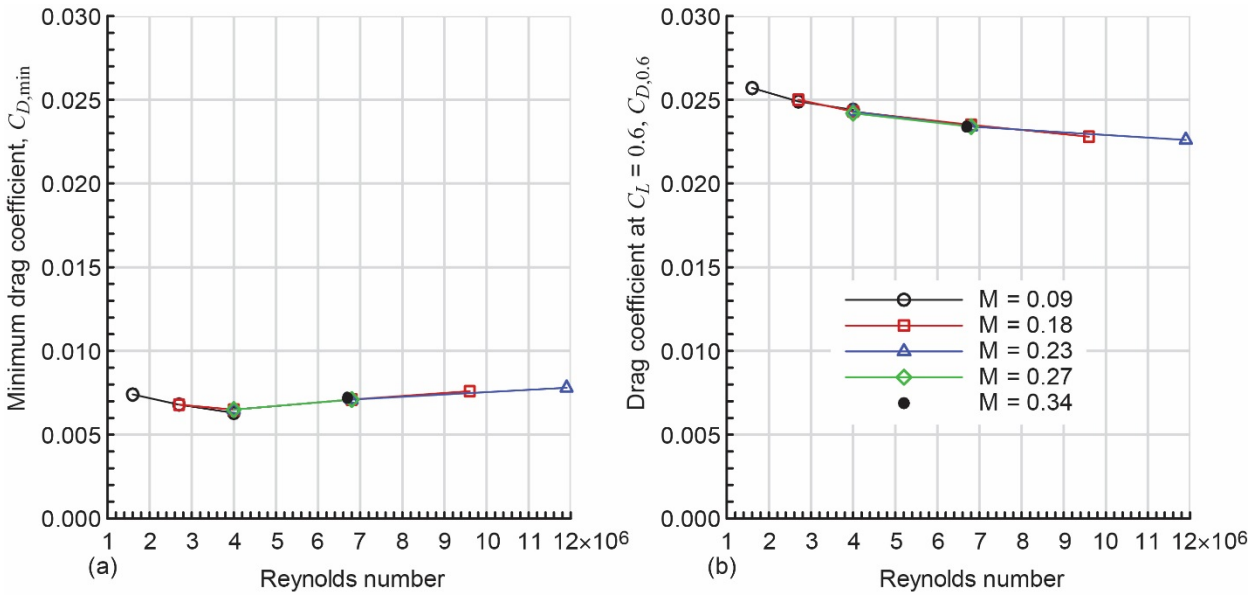

Figure 20.—Effect of Reynolds number on drag coefficients for clean wing for various Mach numbers. (a) Effect on minimum drag coefficient. (b) Effect on C_L = 0.6 drag coefficient.

The variation in drag performance with changes in Reynolds and Mach numbers is summarized in Figure 20 for the clean wing. These plots show immediately that there was no effect of Mach number on $C_{D,min}$ and $C_{D,0.6}$ over the range tested. These results were consistent with the data reported by Edwards and Boltz (Ref. 33), described in the previous paragraph. In terms of Reynolds number dependence, opposite trends were observed for $C_{D,min}$ and $C_{D,0.6}$. The former coefficient exhibited a minimum at Re = 4.0×10^6, as noted earlier in this section, with increasing values measured for increasing Reynolds number. In contrast, $C_{D,0.6}$ was a maximum at the lowest Reynolds number and decreased with increasing Reynolds number.

The performance-based parameter trends shown in Figure 18 to Figure 20 exhibited classic Reynolds and Mach number dependence based upon known comparisons to comparable data in the archival literature. This evaluation of the clean-wing performance thus provides further confidence in the present data set over this range of Re and M. It should be noted for completeness, however, that the typical Reynolds numbers for a CRM65-size airplane are significantly higher. As discussed in Section 2.4, the icing scenarios were based upon holding operations. Wiberg et al. (Ref. 34) provide a summary of the corresponding Reynolds and Mach numbers that range from 24.8×10^6 to 32.9×10^6 and 0.35 to 0.46, respectively. Therefore, the maximum Reynolds number for the present data was at least a factor of two lower than the flight reference conditions. At the maximum Mach number of 0.34, the Reynolds number was nearly a factor of four lower than the flight reference conditions. However, the maximum Mach number of 0.34 was significantly closer to the flight reference conditions. The largest impact of these differences would be in estimating $C_{L,max}$ for the clean-wing configuration. Since both Reynolds and Mach number effects are significant (cf. Figure 19), it is difficult to extrapolate the clean-wing $C_{L,max}$ beyond the acquired data range.

Another implication for the effects of Reynolds and Mach numbers on the performance of the clean wing is the planned comparison between the present data and results from aerodynamic testing conducted at the WSU wind tunnel. Reynolds and Mach numbers cannot be matched between the two wind tunnels because the WSU facility is not pressurized and the CRM65 model was smaller than the F1 wind tunnel model. WSU wind tunnel data were acquired at Re = 0.8×10^6, 1.6×10^6, and 2.4×10^6 with corresponding M = 0.09, 0.18, and 0.27, respectively. Therefore, there was some overlap in the conditions. The data presented in this section show that both Reynolds and Mach numbers must be respected when comparing the clean-wing aerodynamic data from the respective facilities. The companion paper by Lee et al. (Ref. 5) presents these comparisons.

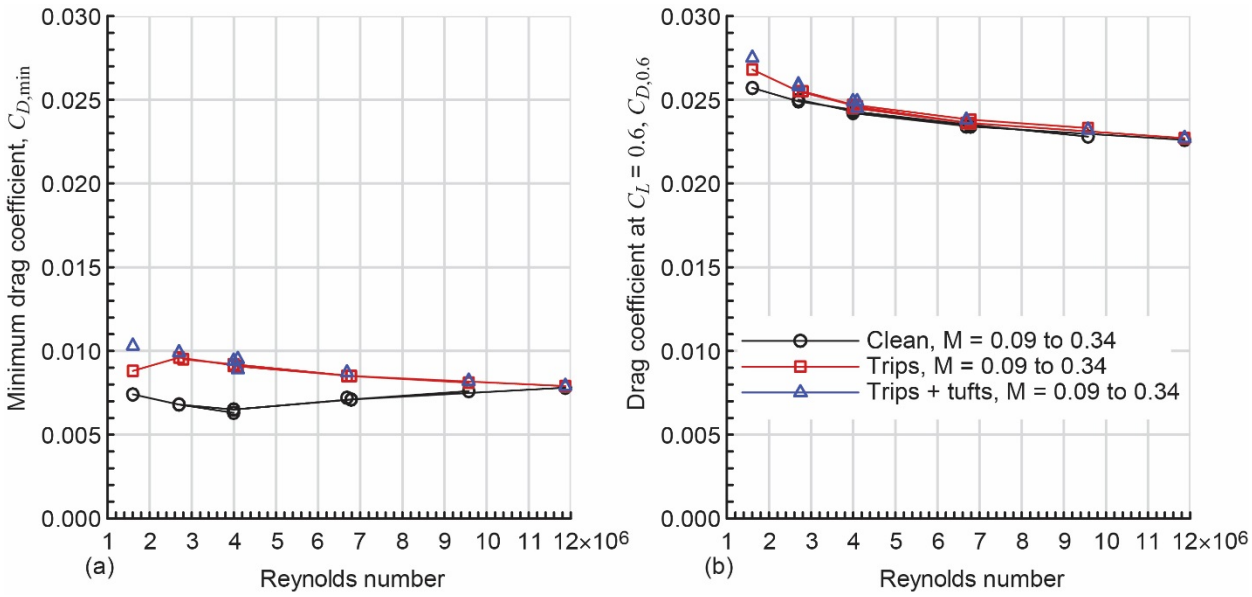

Figure 21.—Effect of boundary-layer trips and mini-tufts on drag coefficients for various Reynolds and Mach numbers. (a) Effect on minimum drag coefficient. (b) Effect on C_L = 0.6 drag coefficient.

3.4 Effect of Boundary-Layer Trips and Mini-Tufts

A series of tests was conducted with boundary-layer trips applied to the model as detailed in Section 2.3. After these tests were completed, the fluorescent mini-tufts were added to the model as detailed in Section 2.5. It was assumed that if there was no measurable effect of the tufts on the wing with boundary-layer trips, then there would be no measurable effect of the tufts on the wing with artificial ice shapes. For all of the runs with trips and with trips plus tufts there was no significant change in lift coefficient relative to the clean wing. This was expected, as the trips and tufts were placed downstream of the leading-edge hilite. For example, the Reynolds and Mach number trends for $C_{L,max}$ were identical to those shown in Figure 18 and Figure 19. The largest changes were observed in the minimum drag coefficient; these changes are illustrated in Figure 21. As Mach number was observed to have little to no effect on drag coefficient, data from all Mach numbers were combined into a single series in Figure 21. This affords a clearer comparison of the Reynolds number effects. The data show that the trips increased $C_{D,min}$ for all but the highest Reynolds number of 11.9×10^6. This was expected, as the trip heights were based upon the lowest Reynolds number, and it was expected that natural boundary-layer transition would move forward to the leading-edge region for higher Reynolds numbers. The trips increased the drag coefficient at C_L = 0.6 up to a Reynolds number of about 4.0×10^6. Only a subset of the Reynolds and Mach number matrix was performed for the wing with mini-tuft applied to the upper surface. Thus, the data points in Figure 21 were not connected with line segments as for the other data. These data show that an additional drag increment due to the tufts was measured for Re = 1.6×10^6. However, this additional drag was small relative to the much larger increases observed for the iced-wing configurations. Therefore, the data show that the presence of the mini-tufts did not have a measurable effect on the iced-wing aerodynamics.

3.5 Iced-Wing Reynolds and Mach Number Results

The pressurization capability of the F1 wind tunnel was fully exploited to investigate the independent effects of Reynolds and Mach numbers on the 13.3-percent-scale wing aerodynamics with the various combinations of high- and low-fidelity artificial ice shapes attached to the wing leading edge. Exemplary results for the effect of Reynolds number at a constant Mach number of 0.18 are plotted in Figure 22 for the wing with the 3D, high-fidelity Maximum Scallop artificial ice shape. These data show that there was

virtually no change in C_L and C_M versus angle of attack as Reynolds number was increased from 2.7×10^6 to 9.5×10^6. The largest changes in performance were observed in drag coefficient. For example, $C_{D,\min}$ decreased by 12 drag counts ($\Delta C_{D,\min} = 0.0012$) as Reynolds number was increased from 2.7×10^6 to 9.5×10^6. Figure 23 provides results from the same configuration as Mach number was increased from 0.09 to 0.27 at constant Re = 4.0×10^6. There was a measurable effect of Mach number on the iced-wing stall; $C_{L,\max}$ and α_{stall} decreased from 0.87° and 18.1° to 0.83° and 16.5°, respectively, as the Mach number was increased from 0.09 to 0.18. For Mach numbers greater than 0.18, there was very little or no variation in $C_{L,\max}$ and α_{stall}. Changes in Mach number from 0.09 to 0.34 had little to no effect on drag coefficient, which is consistent with the data presented previously for the clean wing and wing with boundary-layer trips and mini-tufts.

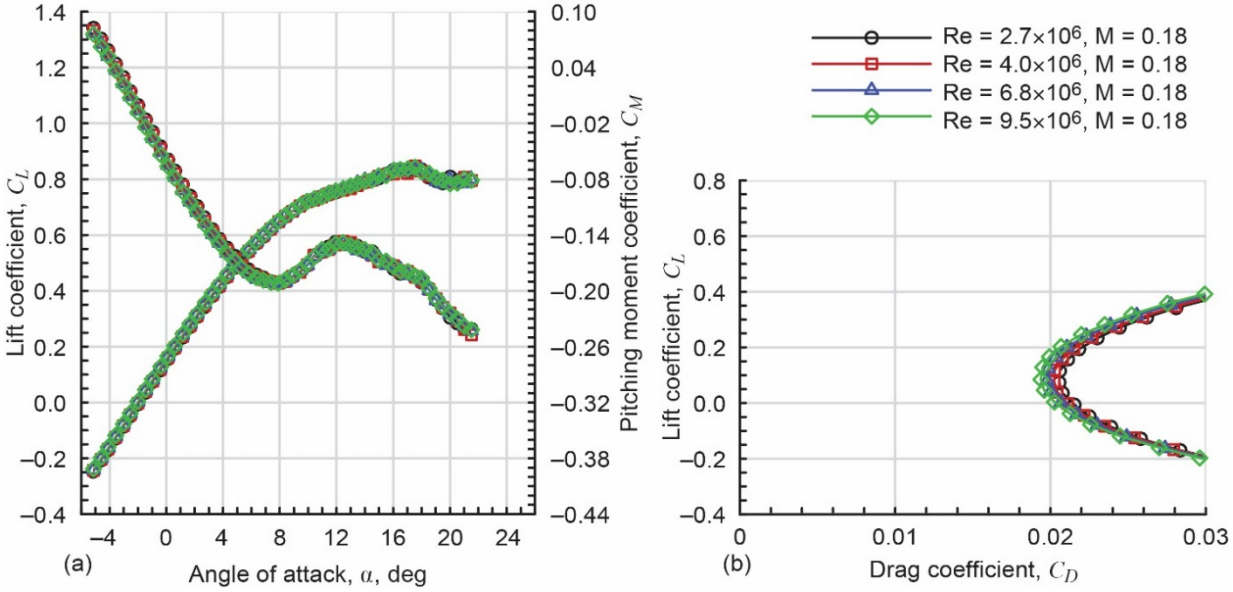

Figure 22.—Effect of Reynolds number on iced-wing performance for 3D, high-fidelity Maximum Scallop artificial ice shape at M = 0.18. (a) Effect on lift and pitching moment coefficient. (b) Effect on drag coefficient.

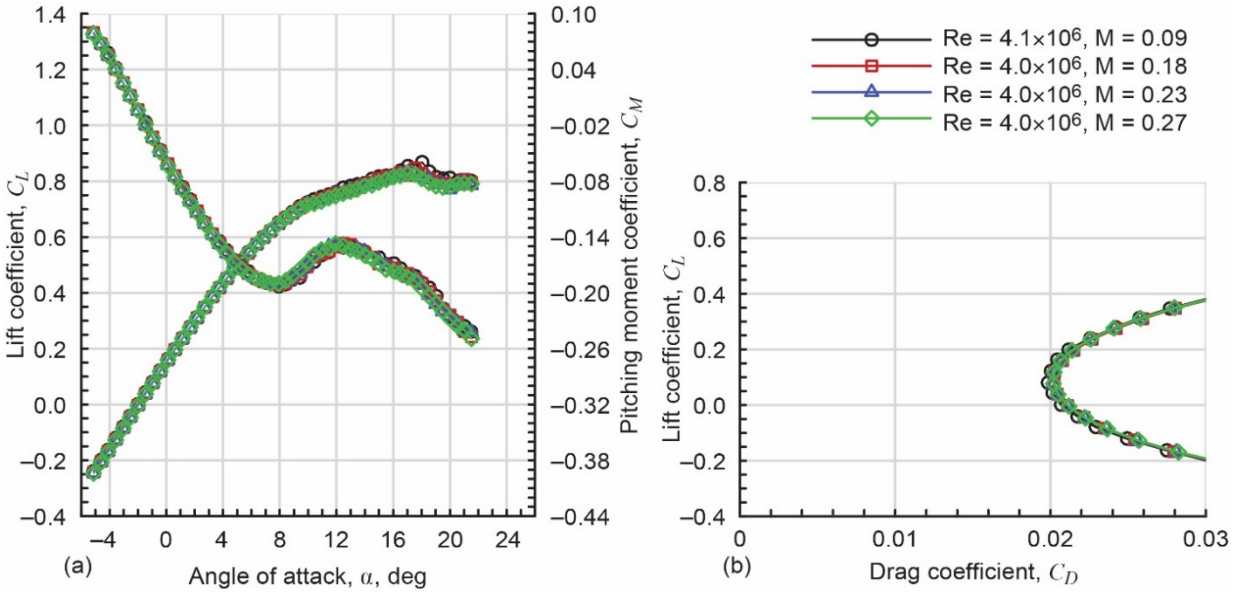

Figure 23.—Effect of Mach number on iced-wing performance for 3D, high-fidelity Maximum Scallop artificial ice shape at Re = 4.0×10^6. (a) Effect on lift and pitching moment coefficient. (b) Effect on drag coefficient.

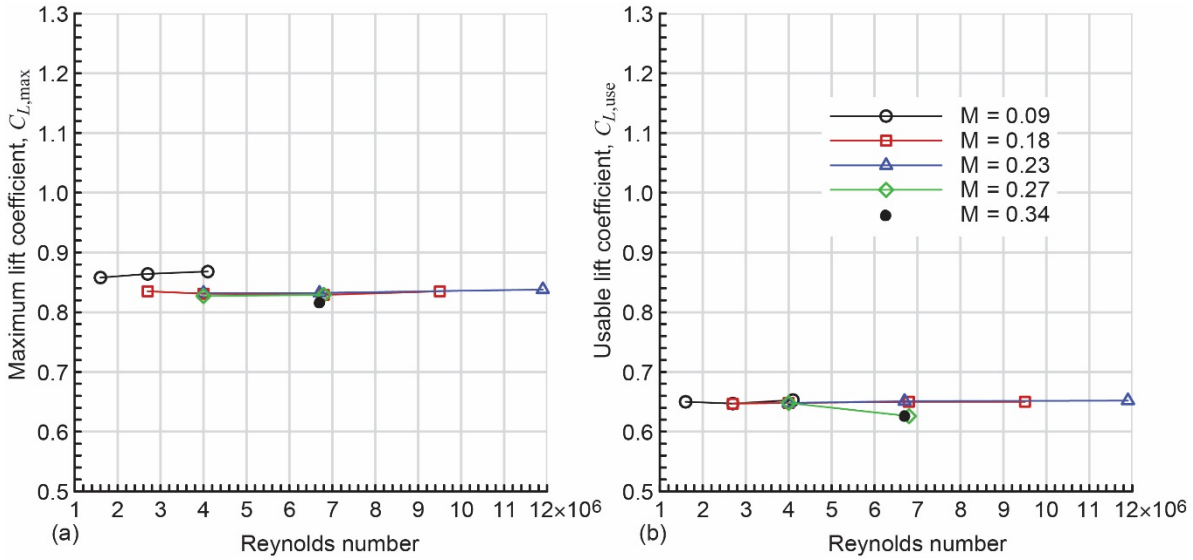

Figure 24.—Effect of Reynolds number on lift coefficients for iced wing with 3D, high-fidelity Maximum Scallop artificial ice shape at various Mach numbers. (a) Effect on maximum lift coefficient. (b) Effect on usable lift coefficient.

The effect of Reynolds and Mach number variation on the iced-wing lift coefficient is summarized in Figure 24 for the 3D, high-fidelity Maximum Scallop configuration. There was an effect of Mach number between 0.09 and 0.18 where $C_{L,max}$ decreased from 0.87 to 0.83 at Re = 4.0×10^6, as noted in the previous paragraph. However, the data show that $C_{L,max}$ was virtually independent of Reynolds number over the range tested. These observations regarding the effects of Reynolds and Mach numbers are consistent with the large volume of iced airfoil data acquired over many years for various airfoils and artificial ice shapes (Refs. 14 and 16). An analogous observation can also be made for $C_{L,use}$, where there was an effect of Mach number at Re = 6.8×10^6, with the value decreasing from 0.65 to 0.63 as Mach number was increased from 0.23 to 0.27. There was no further decrease in $C_{L,use}$ as Mach number was increased to 0.34. The effect of Reynolds number on the minimum and $C_L = 0.6$ drag coefficients is shown in Figure 25 for the Mach number range tested. For the iced-wing configuration, both drag coefficients tended to decrease slightly as Reynolds number was increased.

The results summarized in Figure 24 and Figure 25 hold significant meaning for this research effort. First, the relatively weak effect of Reynolds and Mach numbers on the iced-wing performance suggest that these results could well be extrapolated to the flight reference values described earlier in Section 3.3. Second, these results suggest that testing conducted on the 8.9-percent-scale wing in the WSU wind tunnel are also directly comparable to the present data. The implication from these data for the 8.9-percent-scale model tests at the WSU wind tunnel is that matching of Mach number is more important for the iced-wing configurations than matching of Reynolds number. Of course, these observations are based upon the 3D, high-fidelity Maximum Scallop configuration considered here. The remainder of this section presents data for the other configurations tested to support these observations.

Recall that in Figure 12, aerodynamic performance data were presented for the wing with 3D, high-fidelity artificial ice shapes based upon Maximum Scallop, Small Gap Scallop, and Incomplete Scallop cases. These results showed the effect of ice scallop geometry variation for the selected Re = 11.9×10^6 and M = 0.23 condition. The Reynolds and Mach number effects on this comparison are summarized for the performance-based parameters in Figure 26 for lift coefficient and Figure 27 for drag coefficient. Once again, data from the various Mach numbers has been plotted as a single series for the given configuration. The large range of data for the clean wing was presented for each Mach number individually in Figure 18 to Figure 20. However, for the iced-wing configurations, the dependence of the lift and drag parameters on Reynolds and Mach numbers was significantly reduced, as shown in Figure 26

and Figure 27. The data show that the relative effects of each ice-shape configuration were similar regardless of Reynolds and Mach numbers. For example, the usable lift coefficient associated with the Incomplete Scallop was higher than for the other two configurations over the entire range of Re and M. Furthermore, the relative difference in the values of $C_{L,use}$ was also approximately the same between the Incomplete Scallop and the other two configurations. Admittedly, there was more variation in the $C_{L,use}$ data at lower Re $\leq 4.0\times10^6$ for the Incomplete Scallop configuration that was not present for the other two. In addition, it is the $C_{L,max}$ data at M = 0.09 that shows the largest deviation from the trend established at the higher Mach numbers, as was noted above for the 3D, high-fidelity Maximum Scallop configuration. The relative increments in drag coefficient among the three configurations, plotted in Figure 27, was approximately the same over the entire range of Re and M. These data support the previous conclusion that these results can be compared directly to results from the 8.9-percent-scale model for similar Mach number.

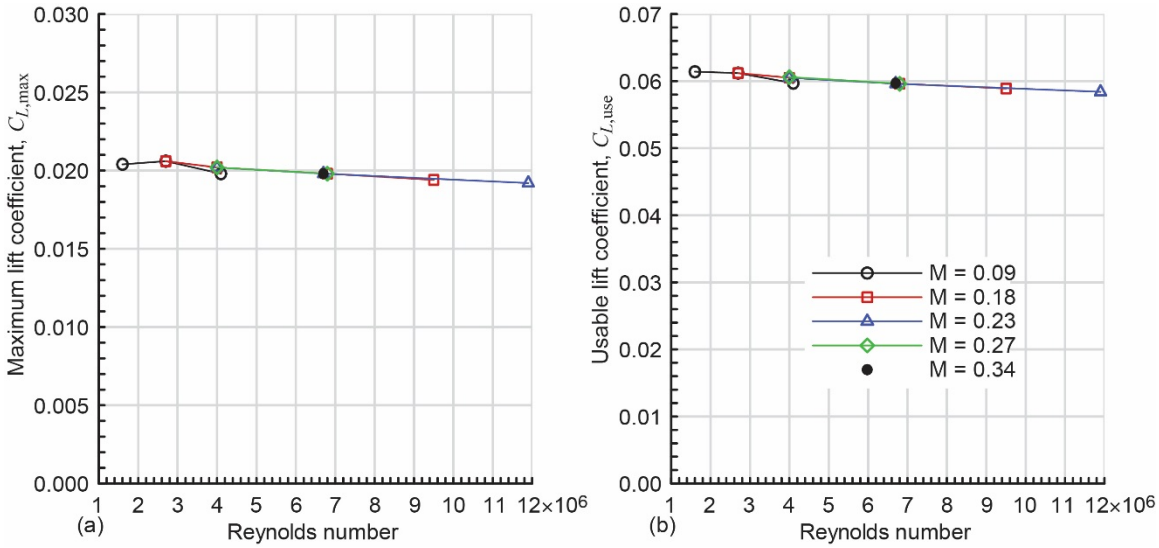

Figure 25.—Effect of Reynolds number on minimum and C_L = 0.6 drag coefficients for iced wing with 3D, high-fidelity Maximum Scallop artificial ice shape at various Mach numbers. (a) Effect on minimum drag coefficient. (b) Effect on C_L = 0.6 drag coefficient.

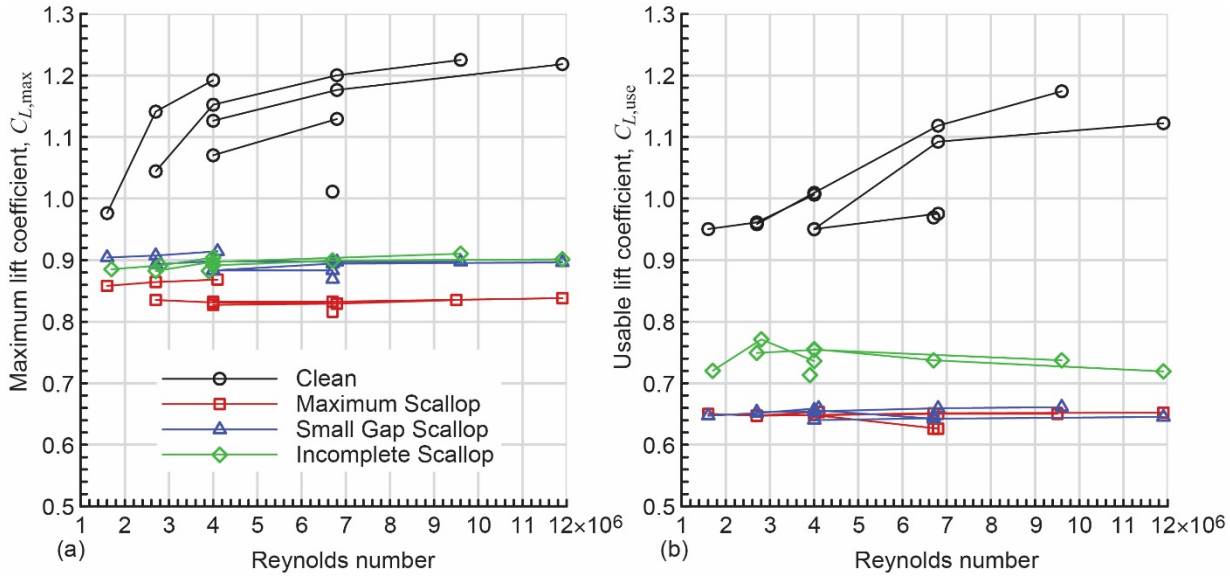

Figure 26.—Effect of Reynolds number on lift coefficients for clean and iced wing with 3D, high-fidelity artificial ice shapes at M = 0.09 to 0.34. (a) Effect on maximum lift coefficient. (b) Effect on usable lift coefficient.

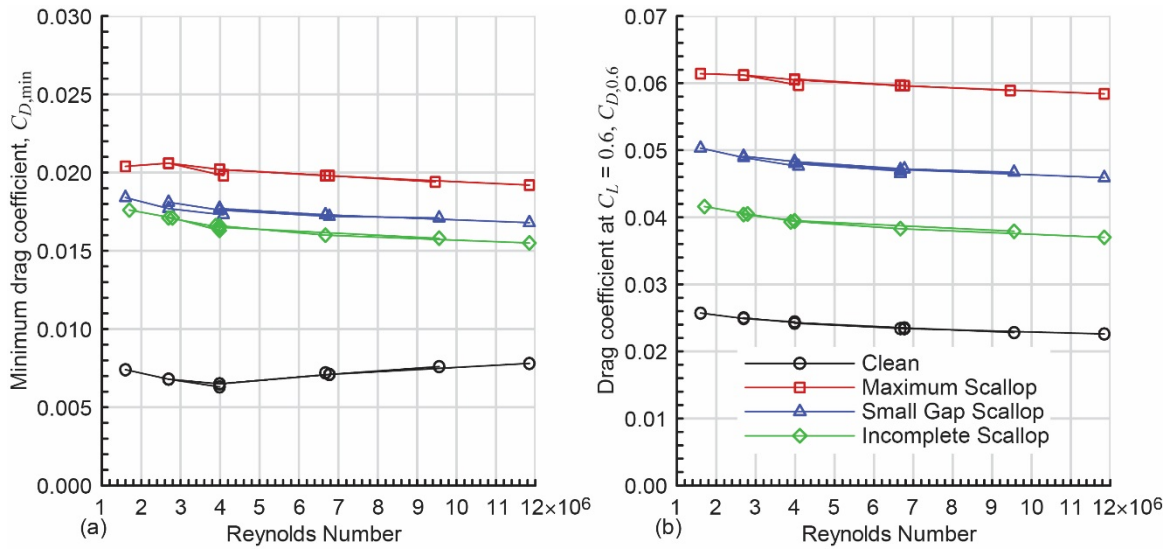

Figure 27.—Effect of Reynolds number on drag coefficients for clean and iced wing with 3D, high-fidelity artificial ice shapes at M = 0.09 to 0.34. (a) Effect on minimum drag coefficient. (b) Effect on C_L = 0.6 drag coefficient.

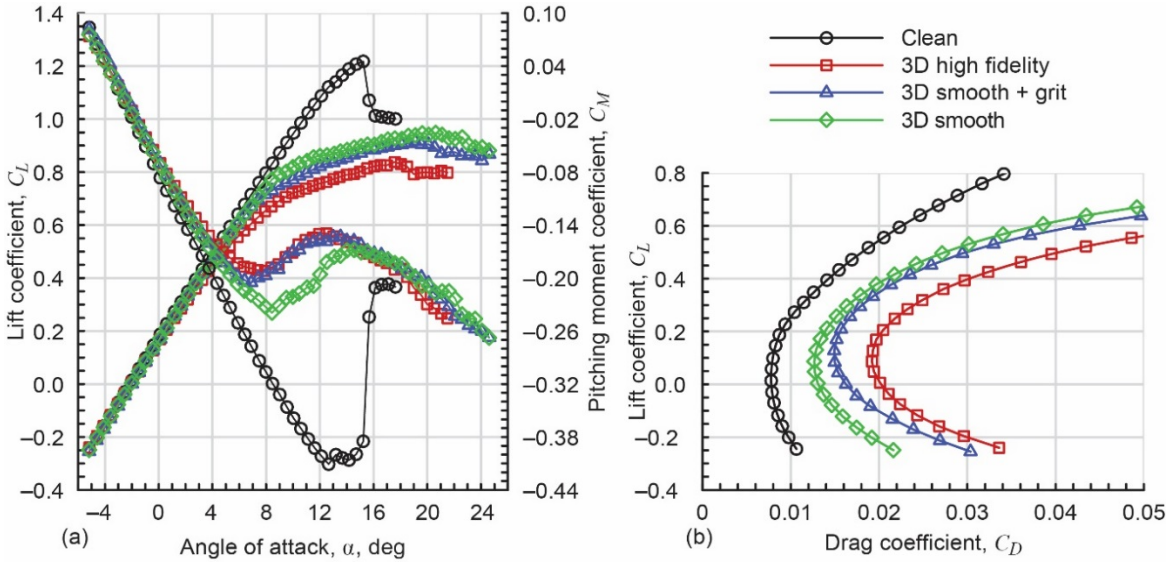

Figure 28.—Comparison of iced-wing performance effects for Maximum Scallop ice shape with varying levels of fidelity at Re = 11.9×10^6 and M = 0.23. (a) Effect on lift and pitching moment coefficient. (b) Effect on drag coefficient.

As described in Section 2.4, lower fidelity versions of the Maximum Scallop, WB33, and Streamwise/Rime ice shapes were also developed and tested because it is important to understand how variations in Reynolds and Mach numbers affect lower fidelity artificial ice shapes. An example case showing the variation in C_L, C_M, and C_D over the entire angle of attack range is presented in Figure 28 for Maximum Scallop configurations at Re = 11.9×10^6 and M = 0.23. Immediately apparent from these data are the significant differences in performance for three versions of the same ice shape. The 3D, high-fidelity version that maintained all of the highly 3D scallop features had the most adverse impact on C_L and C_D. Not surprisingly, when these 3D features are reduced to a smoothed shape (e.g., see Figure 11), the iced-wing performance improves substantially, although the degradations from the clean wing are still significant. Finally, the addition of grit roughness to the 3D smooth configuration shows mixed results. The impact of the grit had only a minor effect on C_L and C_D. However, the grit had a large effect on the usable lift coefficient as associated with the minimum C_M where $C_{L,use}$ decreased from 0.77 to 0.67 with

the addition of grit to the 3D smooth ice shape. The value of $C_{L,use}$ = 0.67 was comparable to the value of 0.65 for the wing with the 3D, high-fidelity artificial ice shape.

The effect of ice shape geometric fidelity for the Maximum Scallop case is summarized in terms of the performance-based parameters in Figure 29 and Figure 30 for the entire range of Re and M tested. For $C_{L,max}$ and $C_{L,use}$, the effects of Reynolds and Mach numbers were similar between the 3D, high-fidelity and the 3D smooth-plus-grit configurations, whereas the values for the 3D smooth configuration showed significantly more dependence upon Reynolds and Mach numbers. In particular, the values of $C_{L,use}$ for the 3D smooth configuration exhibited strong dependence upon Reynolds and Mach numbers. The variation in $C_{D,min}$ and $C_{D,0.6}$, however, exhibited typical Reynolds and Mach number trends, as shown in Figure 27, where there was virtually no effect of Mach number and a small effect of decreasing drag with increasing Reynolds number.

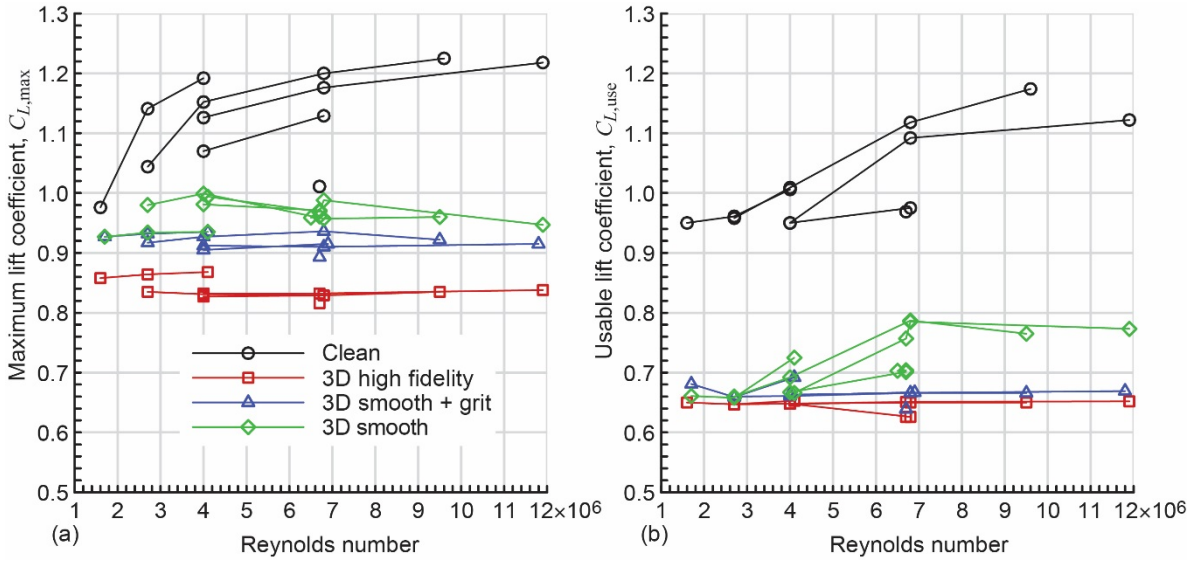

Figure 29.—Effect of Reynolds number on lift coefficients for clean and iced wing with Maximum Scallop artificial ice shapes having various levels of geometric fidelity at M = 0.09 to 0.34. (a) Effect on maximum lift coefficient. (b) Effect on usable lift coefficient.

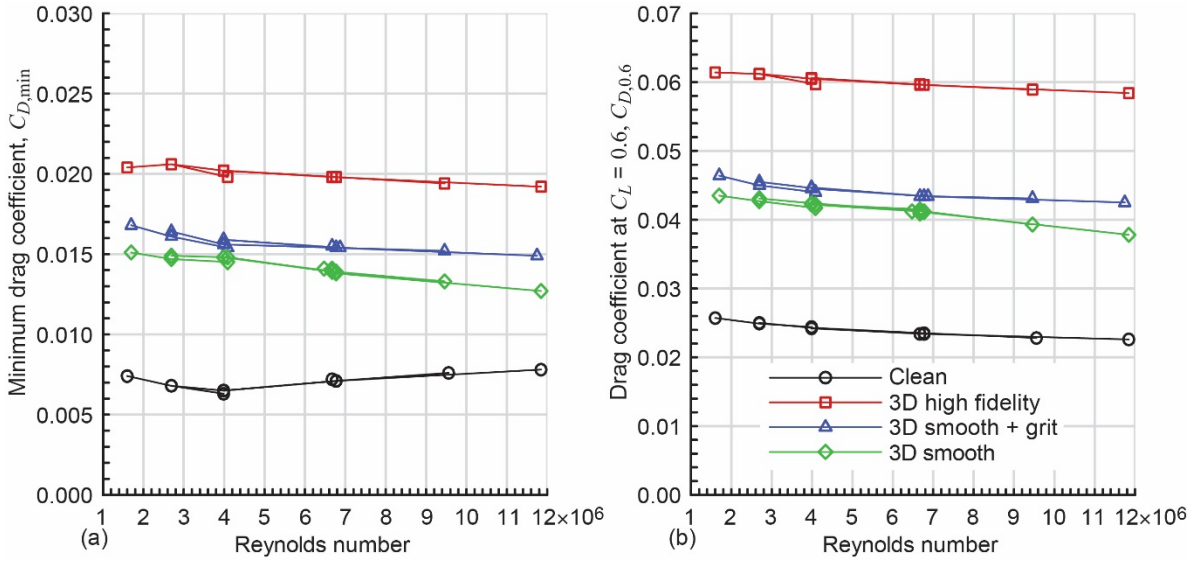

Figure 30.—Effect of Reynolds number on drag coefficients for clean and iced wing with Maximum Scallop artificial ice shapes having various levels of geometric fidelity at M = 0.09 to 0.34. (a) Effect on minimum drag coefficient. (b) Effect on C_L = 0.6 drag coefficient.

As discussed at the beginning of this section in connection with Figure 13, the deleterious aerodynamic effects of the 3D, high-fidelity versions of the Maximum Scallop and WB33 cases were similar in magnitude at Re = 11.9×10^6 and M = 0.23. The effect of varying geometric fidelity for the WB33 case over the entire range of Re and M tested is summarized in Figure 31 for lift coefficient and Figure 32 for drag coefficient. In terms of $C_{L,\max}$, these data were similar to the Maximum Scallop case, where the lower fidelity simulations had higher values that showed little dependence upon Reynolds number. Also similar was the effect of Mach number between 0.09 and 0.18. As for $C_{L,\text{use}}$, there was very little dependence upon Reynolds and Mach numbers for the lower fidelity versions of the WB33 icing case. The increments in drag coefficient summarized in Figure 32 were very similar to those shown for the Maximum Scallop case in Figure 30, as was the slight dependence upon Reynolds number.

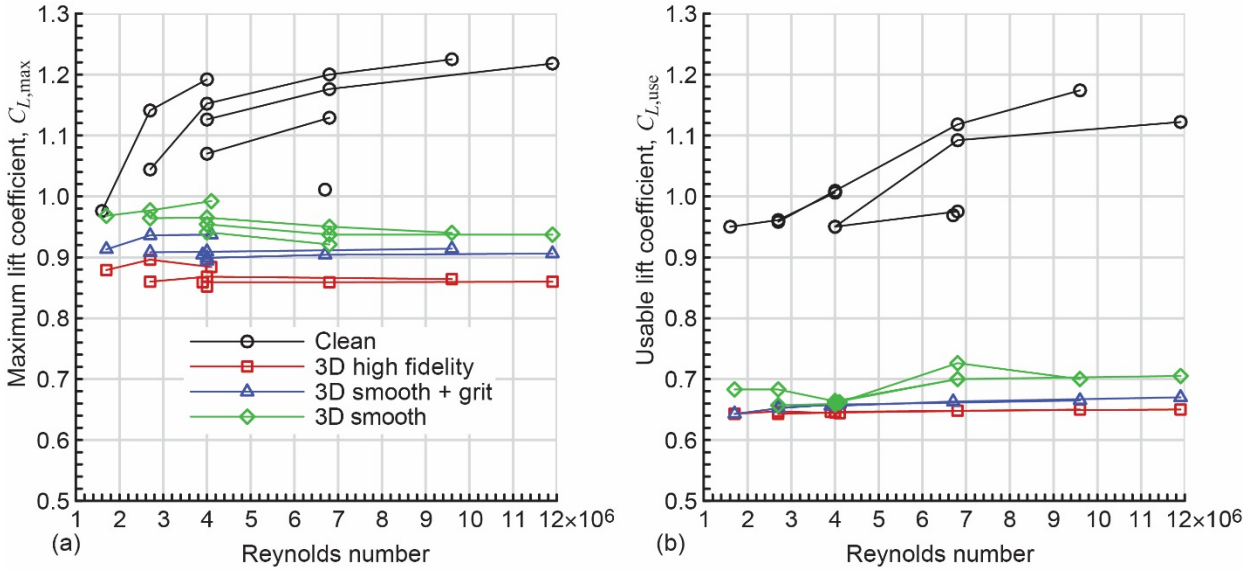

Figure 31.—Effect of Reynolds number on lift coefficients for clean and iced wing with WB33 artificial ice shapes having various levels of geometric fidelity at M = 0.09 to 0.27. (a) Effect on maximum lift coefficient. (b) Effect on usable lift coefficient.

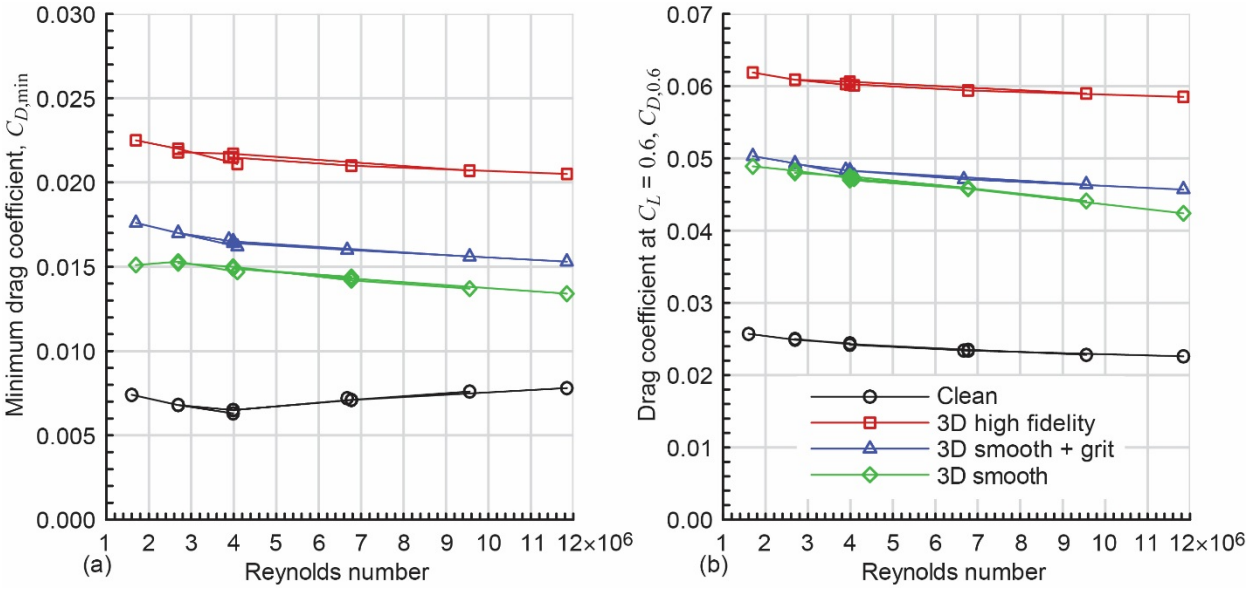

Figure 32.—Effect of Reynolds number on drag coefficients for clean and iced wing with WB33 artificial ice shapes having various levels of geometric fidelity at M = 0.09 to 0.27. (a) Effect on minimum drag coefficient. (b) Effect on C_L = 0.6 drag coefficient.

The Maximum Scallop and WB33 ice-shape cases were large and highly 3D geometries (cf. Figure 4, Figure 8, and Figure 10). It was expected that for these cases, the lower fidelity configurations would not reproduce the aerodynamic effect of the corresponding 3D, high-fidelity configuration even with the addition of grit roughness to the basic 3D smooth geometry. Looking at the ice-shape cross sections shown in Figure 10 for these cases, the corresponding equivalent type of ice on a straight wing is a glaze or horn type of ice shape, for which a large volume of aerodynamic data has been acquired. As described by Bragg, Broeren, and Blumenthal (Ref. 14) for horn ice shapes, the use of simplified smooth cross-sectional geometries led to reductions in maximum lift coefficient similar to those observed for the fully 3D, high-fidelity ice shape. This conclusion is definitely not applicable for the types of swept-wing ice shapes considered here, where there is simply a larger degree of 3D variation in the ice geometry and features. This result represents a fundamental difference from the past research with glaze-horn-type leading-edge ice shapes on straight wings and airfoils.

In contrast to these large shapes, the Streamwise/Rime case was significantly smaller in cross-sectional size (cf. Figure 10) and had significantly smaller 3D features (cf. Figure 7). The effect of varying ice-shape fidelity on lift and drag coefficients is summarized in Figure 33 and Figure 34 over the Re and M range tested. In terms of $C_{L,\max}$, the addition of grit to the 3D smooth geometry resulted in lower values relative to both the 3D, high-fidelity and 3D smooth configurations. Furthermore, $C_{L,\max}$ for the 3D smooth configuration exhibited significant Reynolds number dependence up to 4.0×10^6. Looking at the usable lift coefficient, it is difficult to ascertain any clear trend. This resulted from the inability to define a clear minimum value of C_M, as discussed earlier in Section 3.2. The Reynolds number trends in the drag coefficients plotted in Figure 34 were typical of those shown previously. However, there was a clear difference from the larger ice shapes, where the addition of grit to the 3D smooth configuration resulted in higher drag coefficients than the 3D, high-fidelity configuration. This suggested that the grit size used was too large; however, performing a grit-size optimization study was not an objective of this work. The results do suggest that as long as some roughness level is maintained in the Streamwise/Rime ice shape, low-Reynolds number data can be extrapolated to higher Reynolds number.

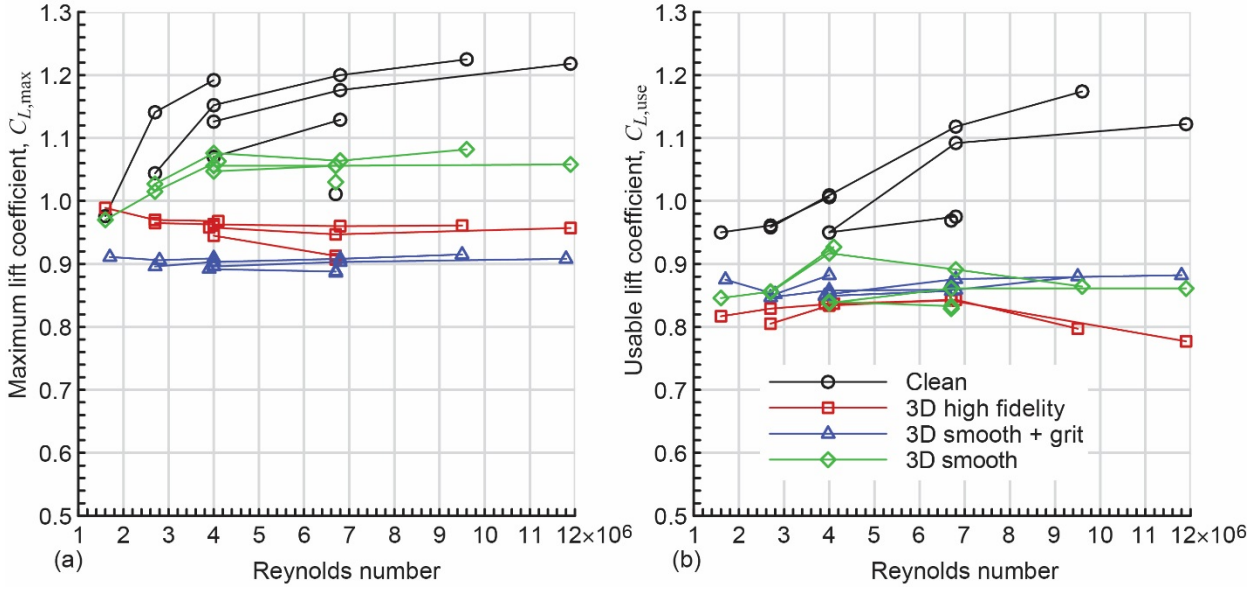

Figure 33.—Effect of Reynolds number on lift coefficients for clean and iced wing with Streamwise/Rime artificial ice shapes having various levels of geometric fidelity at M = 0.09 to 0.34. (a) Effect on maximum lift coefficient. (b) Effect on usable lift coefficient.

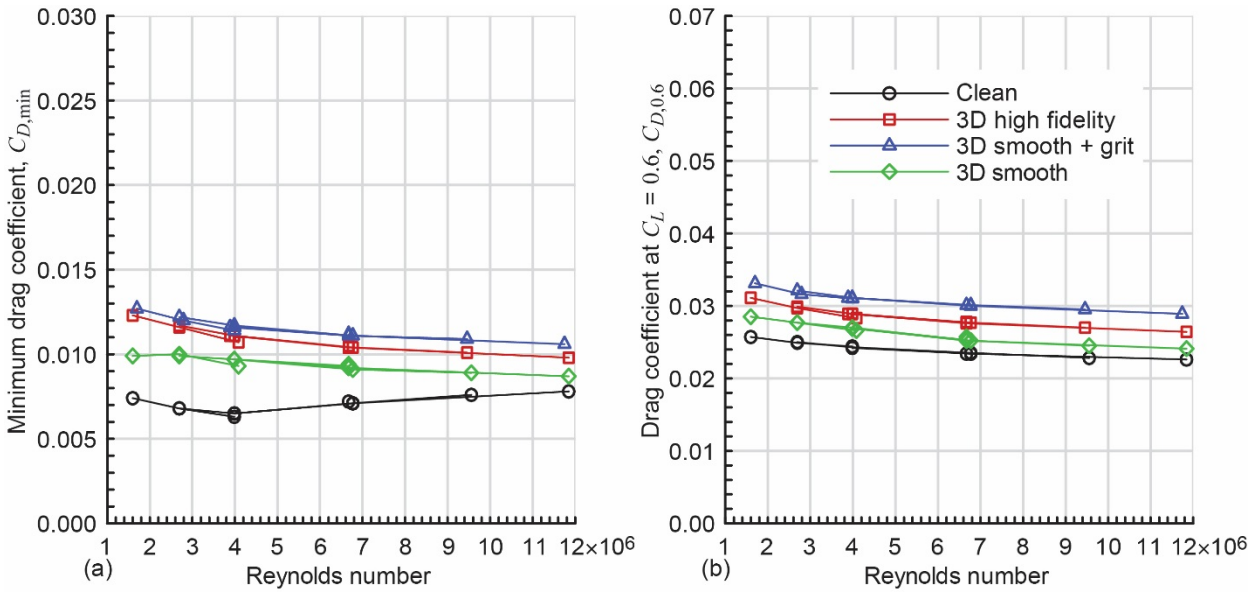

Figure 34.—Effect of Reynolds number on drag coefficients for clean and iced wing with Streamwise/Rime artificial ice shapes having various levels of geometric fidelity at M = 0.09 to 0.34. (a) Effect on minimum drag coefficient. (b) Effect on C_L = 0.6 drag coefficient.

4.0 Summary and Conclusion

This paper presents the results of high-Reynolds number aerodynamic testing of a swept wing with full-span, leading-edge artificial ice shapes. The objectives of this work were to quantify the effects of Reynolds and Mach numbers on clean- and iced-wing performance and to determine fundamental differences from the large volume of past research for iced airfoils and straight wings. Aerodynamic performance testing was conducted at the Office National d'Etudes et de Recherches Aérospatiales (ONERA) F1 wind tunnel using a 13.3-percent-scale semispan wing model of the CRM65, which was based upon the Common Research Model. The artificial ice shapes were based upon three-dimensional (3D) scans of ice accretion in the NASA Icing Research Tunnel and fabricated with rapid-prototype manufacturing. Angle-of-attack sweeps were performed over a Reynolds number range of 1.6×10^6 to 11.9×10^6 and a Mach number range of 0.09 to 0.34. Force balance and surface pressure data were acquired. Mini-tuft flow visualization was also performed during the performance sweeps. Five different ice-shape configurations were investigated using fully 3D, high-fidelity simulations that maintain nearly all of the 3D ice-accretion features documented in previous icing wind tunnel tests. These large, leading-edge ice shapes were nominally based upon airplane holding in icing conditions scenarios. For three of these configurations, lower fidelity simulations were also built and tested. The lower fidelity artificial ice shapes were lofted in the spanwise direction and thus did not contain the large roughness, ice-feather features, or scallop features of the real ice accretion.

The conclusions regarding the effect of Reynolds and Mach numbers on aerodynamic performance were based upon the analysis of four parameters defined in this paper: maximum lift coefficient $C_{L,max}$, usable lift coefficient $C_{L,use}$, minimum drag coefficient $C_{D,min}$, and drag coefficient at a lift coefficient equal to 0.6, $C_{D,0.6}$. The usable lift coefficient was based upon an analysis of the wing pitching moment as indicative of stall progression on the wing. This parameter was developed because in many cases for the iced-wing configurations, the stalling angle associated with maximum lift was higher than the clean-wing stall angle. This represents a fundamental difference from past research on straight wings or airfoils with large, leading-edge artificial ice shapes, where the stall angle was typically lower than the clean value.

Results for the clean-wing configuration showed a strong dependence of $C_{L,\max}$ and $C_{L,\text{use}}$ on both Reynolds and Mach numbers. This observation is consistent with past research for straight wings and airfoils and with two applicable swept-wing studies cited in this paper. Because of this dependence, it is difficult to extrapolate the clean-wing lift performance to flight Reynolds and Mach numbers for airplane holding conditions. No effect of Mach number was observed for $C_{D,\min}$ and $C_{D,0.6}$. The Reynolds number effects on the drag parameters were fairly weak and may allow for extrapolation to flight Reynolds number for holding conditions. The clean-wing configuration results also show that both Reynolds number and Mach number must be respected when making comparisons to smaller scale model wind tunnel tests at the lower range of Re and M.

Results for the iced-wing configurations with the 3D, high-fidelity artificial ice shapes exhibited consistent Reynolds and Mach number trends. In terms of the lift-based parameters, $C_{L,\max}$ and $C_{L,\text{use}}$ showed little to no dependence upon Reynolds number and Mach number greater than 0.18. These results agreed with the past research on iced airfoils. This lack of Reynolds and Mach number dependence means that the present results may be extrapolated to flight in holding conditions. Furthermore, testing conducted with artificial ice shapes on smaller scale models at the lower range of Re and M can yield very meaningful results with the caveat that possible Mach number effects should be considered for $M < 0.18$. In terms of drag-based parameters, there was no Mach number effect, and only little Reynolds number effect whereby both $C_{D,\min}$ and $C_{D,0.6}$ decreased slightly with increased Re.

The effect of ice-shape fidelity was investigated for three of five configurations. The 3D smooth, lower fidelity ice shapes did not contain any ice roughness features. These roughness features were simulated with another set of ice shapes whereby 46-grit-size silicon carbide grains were added to the baseline 3D smooth ice shapes. In general, the Reynolds and Mach number trends in both lift and drag coefficients for the wing with the lower fidelity artificial ice-shape configurations were consistent with the results for the wing with the high-fidelity artificial ice shapes. Under some conditions, the wing performance with the 3D smooth configurations did exhibit more Reynolds number dependence than was observed when grit was added and for the high-fidelity artificial ice shapes. This suggests that the addition of grit roughness to smooth shapes is important for both extrapolation of data to higher Reynolds number and comparison to smaller scale model tests.

Two of the three icing cases, Maximum Scallop and WB33, had cross sections similar to glaze-horn-type ice and were characterized by large-scale 3D ice features. The results showed significant differences in aerodynamic performance for the wing with the lower fidelity versions of these cases. This result represents a fundamental difference from the past research with glaze-horn-type leading-edge ice shapes on straight wings and airfoils, where lower fidelity versions tended to have aerodynamic penalties similar to those of their fully 3D, high-fidelity counterparts. This conclusion was anticipated because swept-wing ice accretion is typically characterized by greater three-dimensionality. The present data have quantified these differences aerodynamically.

The results presented in this paper have demonstrated that while Reynolds and Mach number effects are important for quantifying the clean-wing performance, there is very little to no effect for an iced-wing with 3D, high-fidelity artificial ice shapes or 3D smooth ice shapes with grit roughness. These conclusions are consistent with the large volume of past research on iced airfoils. However, some differences were also noted for the associated stalling angle of the iced swept wing and for various lower fidelity versions of the leading-edge ice accretion. More research is planned to further investigate the key features of ice-accretion geometry that must be simulated in lower fidelity versions in order to capture the essential aerodynamics.

References

1. Broeren, Andy P., et al.: Swept-Wing Ice Accretion Characterization and Aerodynamics. AIAA–2013–2824 (NASA/TM—2013-216555), 2013. http://ntrs.nasa.gov
2. Broeren, Andy P., et al.: Ice-Accretion Test Results for Three-Large-Scale Swept-Wing Models in the NASA Icing Research Tunnel. AIAA–2016–3733 (NASA/TM—2016-219137), 2016. http://ntrs.nasa.gov
3. Fujiwara, Gustavo E.C., et al.: Computational and Experimental Ice Accretions of Large Swept Wings in the Icing Research Tunnel. AIAA–2016–3734, 2016.
4. Radenac, Emmanuel: Validation of a 3D Ice Accretion Tool on Swept Wing of the SUNSET2 Program. AIAA–2016–3735, 2016.
5. Lee, Sam, et al.: Comparison of Iced Aerodynamic Measurements on Swept Wing From Two Wind Tunnels. AIAA–2018–3493, 2018.
6. Woodard, Brian S., et al.: Summary of Ice Shape Geometric Fidelity Studies on an Iced Swept Wing. AIAA–2018–3494, 2018.
7. Sandhu, Navdeep, et al.: Effect of Simulated Scalloped Ice on the Aerodynamics of a Swept-Wing at Low-Reynolds Number. AIAA–2018–3495, 2018.
8. Broeren, Andy P., et al.: Aerodynamic Simulation of Ice Accretion on Airfoils. NASA/TP—2011-216929, 2011. http://ntrs.nasa.gov
9. Broeren, Andy P., et al.: Validation of 3-D Ice Accretion Measurement Methodology for Experimental Aerodynamic Simulation. NASA/TM—2015-218724 (AIAA–2014–2614), 2015. http://ntrs.nasa.gov
10. Morgan, Harry L., Jr.; Ferris, James C.; and McGhee, Robert J.: A Study of High-Lift Airfoils at High Reynolds Numbers in the Langley Low-Turbulence Pressure Tunnel. NASA TM–89125, 1987. http://ntrs.nasa.gov
11. Addy, Harold E., Jr.; and Chung, James J.: A Wind Tunnel Study of Icing Effects on a Natural Laminar Flow Airfoil. AIAA–2000–0095 (NASA/TM—2000-209775), 2000. http://ntrs.nasa.gov
12. Addy, Harold E., Jr.: Ice Accretions and Icing Effects for Modern Airfoils. NASA/TP—2000-210031 (DOT/FAA AR–99/89), 2000. http://ntrs.nasa.gov
13. Addy, Harold E., Jr., et al.: A Wind Tunnel Study of Icing Effects on a Business Jet Airfoil. AIAA–2003–0727 (NASA/TM—2003-212124), 2003. http://ntrs.nasa.gov
14. Bragg, M.B.; Broeren, A.P.; and Blumenthal, L.A.: Iced-Airfoil Aerodynamics. Prog. Aerosp. Sci., vol. 41, no. 5, 2005, pp. 323–418.
15. Broeren, Andy P.; Bragg, Michael B.; and Addy, Harold E., Jr.: Effect of Intercycle Ice Accretions on Aerodynamic Performance. J. Aircraft, vol. 41, no. 1, 2004, pp. 165–174.
16. Broeren, Andy P., et al.: Effect of High-Fidelity Ice Accretion Simulations on the Performance of a Full-Scale Airfoil Model. J. Aircraft (NASA/TM—2010-216344), vol. 47, no. 1, 2010, pp. 240–254. http://ntrs.nasa.gov
17. Vassberg, John C., et al.: Development of a Common Research Model for Applied CFD Validation Studies. AIAA–2008–6919, 2008.
18. Rivers, Melissa B.; and Dittberner, Ashley: Experimental Investigation of the NASA Common Research Model (Invited). AIAA–2010–4218, 2010.
19. Rivers, Melissa B.; and Dittberner, Ashley: Experimental Investigations of the NASA Common Research Model in the NASA Langley National Transonic Facility and the NASA Ames 11-Ft Transonic Wind Tunnel (Invited). AIAA–2011–1126, 2011.
20. Vassberg, John C., et al.: Summary of the Fourth AIAA CFD Drag Prediction Workshop. AIAA–2010–4547, 2010.
21. Torz-Dupuis, L.: Test NASA SUNSET II of the CRM65 Wing Model Representative of the CRM65 Wing at 1/7.5 on Half Model Set-Up in the ONERA F1 Wind Tunnel. ONERA Report No. PV 4/23611 DMPE/DSFM, 2017.

22. Coleman, Hugh W.; and Steele, W. Glenn: Experimentation and Uncertainty Analysis for Engineers. Wiley-Interscience, New York, NY, 1989, pp. 40–118.
23. Kline, S.J.; and McClintock, F.A.: Describing Uncertainties in Single-Sample Experiments. Mechanical Engineering, vol. 75, no. 1, 1953, pp. 3–8.
24. Broeren, Andy P., et al.: Low-Reynolds Number Aerodynamics of an 8.9 Percent Scale Semispan Swept Wing for Assessment of Icing Effects. AIAA–2017–4372 (NASA/TM—2017-219533), 2017. http://ntrs.nasa.gov
25. Camello, Stephanie C., et al.: Effect of Ice-Shape Fidelity on Swept-Wing Aerodynamic Performance. AIAA–2017–4373, 2017.
26. Woodard, Brian S., et al.: Preliminary Testing of Low Reynolds Number Aerodynamics for a Swept Wing With Artificial Ice Roughness. DOT/FAA/TC–17/48, 2017.
27. Barlow, Jewel B.; Rae, William H., Jr.; and Pope, Alan: Low-Speed Wind Tunnel Testing. Third ed., John Wiley & Sons, Inc., 1999, pp. 367–425.
28. National Institute for Aviation Research: Data Reduction System: Boundary Corrections Three Dimensional Aircraft. Walter H. Beech Wind Tunnel Engineering Process Description, 2014. Available from Wichita State University.
29. Camello, Stephanie C., et al.: Generation of Fullspan Leading-Edge 3D Ice Shapes for Swept-Wing Aerodynamic Testing. AIAA–2016–3737, 2016.
30. Furlong, G. Chester; and McHugh, James G.: A Summary and Analysis of the Low-Speed Longitudinal Characteristics of Swept Wings at High Reynolds Number. NACA TR–1339, 1957. http://ntrs.nasa.gov
31. Lynch, Frank T.; and Khodadoust, Abdollah: Effects of Ice Accretions on Aircraft Aerodynamics. Prog. Aerosp. Sci., vol. 37, no. 8, 2001, pp. 669–767.
32. Koven, William; and Graham, Robert R.: Wind-Tunnel Investigation of High-Lift and Stall-Control Devices on a 37° Sweptback Wing of Aspect Ratio 6 at High Reynolds Number. NACA RM–L8D29, 1948. http://ntrs.nasa.gov
33. Edwards, George G.; and Boltz, Frederick W.: An Analysis of the Forces and Pressure Distribution on a Wing With the Leading Edge Swept Back 37.25°. NACA RM–A9K01, 1950. http://ntrs.nasa.gov
34. Wiberg, Brock D., et al.: Large-Scale Swept-Wing Icing Simulations in the NASA Glenn Icing Research Tunnel Using LEWICE3D. AIAA–2014–2617, 2014.